INTERNATIONAL JOURNAL FOR NUMERICAL METHODS IN FLUIDS, VOL. 9, 651–688 (1989)

LOW REYNOLDS NUMBER HYDRODYNAMIC INTERACTION OF A SOLID PARTICLE WITH A PLANAR WALL

E. P. ASCOLI

Department of Chemical Engineering, California Institute of Technology, Pasadena, California 91125, U.S.A.

D. S. DANDY

Sandia National Laboratories, Livermore, California 94550, U.S.A.

AND

L. G. LEAL

Department of Chemical Engineering, California Institute of Technology, Pasadena, California 91125, U.S.A.

SUMMARY

The slow viscous flow problem of an arbitrary solid particle in motion near a planar wall is recast into a boundary integral formulation. The present formulation employs the Green function appropriate to the planar wall problem and is developed in sufficient generality to allow calculations for arbitrary particles in any base flow which satisfies Stokes equations and no-slip on the wall. The resulting integral equations are easily discretized and solved for the particle surface tractions. Calculations are performed for axisymmetric motions of a variety of ellipsoids near the planar wall. Agreement with existing theory is excellent.

KEY WORDS Stokes flow Creeping flow Wall Green function Boundary integral method

INTRODUCTION

Knowledge of the hydrodynamic resistance of a solid body moving slowly through a viscous liquid is of importance in understanding a wide variety of low Reynolds number sedimentation phenomena. The majority of slow viscous flow resistance calculations have focused on situations where the fluid medium extends to infinity in all directions. In all real situations, however, the fluid is externally bounded by rigid walls or free surfaces. When these external boundaries are located at finite distances from the particle, they can have significant effects on the particle motion. A variety of authors have theoretically considered the effects of walls on the creeping motion of small solid particles for specific cases where the particle and wall geometries are simple. In particular, Brenner[1] used bipolar co-ordinates to obtain 'exact' corrections to Stokes drag for a solid sphere moving perpendicular to a solid wall for the full range of wall-to-sphere distances. Wakiya[2] considered slow viscous flow past ellipsoids between two parallel walls. For more general geometries, asymptotic theory has been developed using the method of reflections when the particle is, in some sense, far from the wall. For example, Brenner[3,4] and Cox and Brenner[5] have considered the problem of an arbitrary particle in the limiting case that the ratio of particle

0271-2091/89/060651-38$19.00

Received 18 May 1988
Revised 18 August 1988

dimension to the distance from bounding walls is small. At the other extreme, when the particle-to-wall distance is small compared to the particle dimension, classical lubrication theory[6,7] has been applied.

For more general cases, it is most convenient to adopt a numerical method. In particular, for low Reynolds number flows governed by the creeping motion equations, the most efficient approach is the boundary integral method pioneered by Youngren and Acrivos[8] for uniform flow past a solid particle of *arbitrary* shape in an unbounded fluid medium. In their technique, the creeping flow problem was formulated as a system of linear integral equations of the first kind for the distribution of stokeslets over the particle surface. The unknown densities of the stokeslets were exactly the desired particle surface stress forces. Subsequent numerical discretization of the integral system yielded an algebraic system which was easily solved for the particle surface stress forces.

The formulation of Youngren and Acrivos could also be applied to the case of a solid particle moving near a planar wall. Because of their choice of the stokeslet as the fundamental singular solution, however, surface stress forces would need to be determined at the planar wall as well as the particle surface. In general, this would necessitate truncation of the planar wall to a finite region, with subsequent distribution of elements on this finite region. The present work considers an alternative boundary integral formulation of the problem, with the fundamental singular solution, or more accurately the Green function, selected to eliminate the need for determination of surface forces on the planar wall. The formulation will be sufficiently general to allow calculations for arbitrary particles in any base flow that satisfies Stokes equations and the no-slip condition on the planar wall. For simplicity, however, the method is *illustrated* for the specific case of axisymmetric ellipsoidal particles moving perpendicular to the planar wall in an otherwise quiescent fluid.

FORMULATION

Theory

We consider the slow motion of a solid particle in the vicinity of an infinite, no-slip, planar boundary. The suspending fluid is assumed to be Newtonian with constant density. The problem is shown schematically in Figure 1. The analysis presented here is based upon the creeping motion approximation in which the inertial terms in the equations of motion are neglected entirely. The governing equations, in dimensionless form, are thus

$$\mathbf{0} = -\nabla p + \nabla^2 \mathbf{u}, \tag{1}$$

$$0 = \nabla \cdot \mathbf{u}. \tag{2}$$

The boundary conditions are

$$\mathbf{u} \to \mathbf{0} \quad \text{as } \|\mathbf{x}\| \to \infty, \tag{3}$$

$$\mathbf{u} = \mathbf{0} \quad \text{for } \mathbf{x} \in \mathbf{P} = \{\mathbf{x} \in \mathbf{R}^3 : \mathbf{x} = (x, y, z) \text{ and } z = 0\}, \tag{4}$$

and on the surface of the particle

$$\mathbf{u} = \mathbf{u}_s(\mathbf{x}_s) \quad \text{(specified)}. \tag{5}$$

For the case of a solid particle translating in an otherwise quiescent fluid, $\mathbf{u}_s$ is constant on the surface. For the case of an imposed base flow at infinity $\mathbf{u}_b$, p_b, satisfying Stokes equation and the no-slip condition on the planar wall, the variables $\mathbf{u}$ and p in equations (1)–(5) are to be interpreted as disturbance variables, i.e. the actual flow variables minus the base flow.

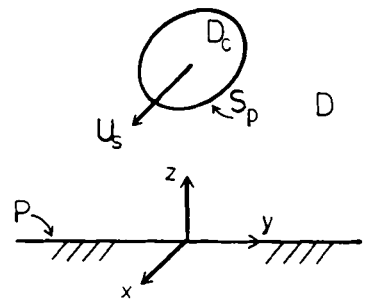

Figure 1. Schematic of the general problem

In the boundary integral method, equations (1) and (2) and the corresponding boundary conditions (3)–(5) are recast into an equivalent integral formulation. The current application of the technique differs from previous applications (general details of the boundary integral formulation are given by Ladyzhenskaya[9]) primarily in the choice of the so-called 'fundamental solution' for the system. The transformation of equations (1)–(5) into integral form is accomplished using the Green formula for the Stokes system:

$$\int_\Omega ((\nabla^2\mathbf{u} - \nabla p)\cdot\mathbf{w} - (\nabla^2\mathbf{w} + \nabla q)\cdot\mathbf{u})\,dV = \int_{\partial\Omega} (\mathbf{n}\cdot\mathbf{T}\cdot\mathbf{w} - \mathbf{n}\cdot\boldsymbol{\Sigma}\cdot\mathbf{u})\,dS, \quad \mathbf{x}\in\Omega, \tag{6}$$

where

$$\mathbf{T} = (\nabla\mathbf{u} + (\nabla\mathbf{u})^{\mathrm{T}}) - p\mathbf{I}, \tag{7}$$

$$\boldsymbol{\Sigma} = (\nabla\mathbf{w} + (\nabla\mathbf{w})^{\mathrm{T}}) + q\mathbf{I}. \tag{8}$$

Equation (6) is valid for *any* sufficiently smooth fields $\mathbf{u}$, p and $\mathbf{w}$, q such that $\mathbf{u}$ and $\mathbf{w}$ are solenoidal. Here Ω is an open subset of $\mathbf{R}^3$ and $\partial\Omega$ is its boundary with outer normal $\mathbf{n}$.* This formula, which relates the Stokes operator to its adjoint operator, is derived by direct application of the divergence theorem and algebraic manipulation. Solutions to appropriately selected adjoint operator systems may be superposed using equation (6).

Thus, in the 'classical' boundary integral formulation, Youngren and Acrivos,[8,10] Lee and Leal[11] and Rallison and Acrivos[12] all used the fundamental solution corresponding to a point force in an *unbounded* Newtonian fluid, i.e. the solution of

$$\delta(\mathbf{x}-\xi)\mathbf{e}_j = \nabla_\xi\hat{q}^j(\xi,\mathbf{x}) + \nabla_\xi^2\hat{\boldsymbol{\phi}}^j(\xi,\mathbf{x}), \quad 0 = \nabla_\xi\cdot\hat{\boldsymbol{\phi}}^j(\xi,\mathbf{x}) \tag{9}$$

subject to the simple additional conditions

$$\hat{\boldsymbol{\phi}}^j(\xi,\mathbf{x}) = O\left(\frac{1}{\|\mathbf{x}-\xi\|}\right) \quad \text{and} \quad \hat{q}^j(\xi,\mathbf{x}) = O\left(\frac{1}{\|\mathbf{x}-\xi\|^2}\right) \quad \text{as} \quad \|\mathbf{x}-\xi\|\to\infty. \tag{10}$$

---

* In the subsequent analysis it will be assumed that to each point of the boundaries of the domains under consideration there corresponds a 'well defined' normal (for instance the boundary is assumed not to have corners or cusps). This constraint may be relaxed in certain situations, resulting in a modification of equations (13)–(14), (21)–(22) and all subsequent equations which derive from them. For more precise mathematical restrictions on Ω and $\partial\Omega$ the reader is referred to References 8 and 9.

This 'fundamental solution' is the so-called stokeslet solution

$$\hat{v}_i^j = -\frac{1}{8\pi}\left\{\frac{\delta_{ij}}{r} + \frac{r_i r_j}{r^3}\right\}, \quad \hat{q}^j = \frac{1}{4\pi}\left\{\frac{r_j}{r^3}\right\}, \quad \hat{\Sigma}_{kl}^j = \frac{3}{4\pi}\left\{\frac{r_k r_l r_j}{r^5}\right\}, \tag{11}$$

where $\mathbf{r} = \xi - \mathbf{x}$. Physically, $\hat{v}_i^j$ is the ith component of the velocity at ξ due to a unit force, or stokeslet, applied at the point $\mathbf{x}$ in the direction $\mathbf{e}_j$. The quantity $-q^j$ is the corresponding pressure. Superposition is performed using equation (6) by identifying $\mathbf{w}$ with $\hat{\mathbf{v}}^j(\xi, \mathbf{x})$, Σ with $\hat{\Sigma}^j$ and q with $\hat{q}^j$. The result is the system of integral equations

$$-(\mathbf{u}(\mathbf{x}))_j = \int_{\partial\Omega} \mathbf{n}\cdot\mathbf{T}(\xi)\cdot\hat{\mathbf{v}}^j(\xi, \mathbf{x})\,dS_\xi - \int_{\partial\Omega} \mathbf{n}\cdot\hat{\Sigma}^j(\xi, \mathbf{x})\cdot\mathbf{u}(\xi)\,dS_\xi, \quad \mathbf{x}\in\Omega \quad \text{for } j = 1, 2, 3. \tag{12}$$

The first integral in equation (12) is termed the single-layer potential and has density $\mathbf{f} = \mathbf{n}\cdot\mathbf{T}$. Similarly, the second integral is called the double-layer potential with density $\mathbf{u}$. Equation (12) provides an integral representation for the solution of Stokes equation in terms of the values of the surface stress and velocity on $\partial\Omega$. However, strictly speaking equation (12) is only valid for $\mathbf{x}\in\Omega$, but in fact the single layer potential is continuous at the boundary while the double layer potential suffers a jump across the boundary given by

$$\lim_{\mathbf{x}\in\Omega\to\mathbf{x}_s}\left\{\int_{\partial\Omega} \mathbf{n}\cdot\hat{\Sigma}^j(\xi, \mathbf{x})\cdot\mathbf{u}(\xi)\,dS_\xi\right\} = \tfrac{1}{2}(\mathbf{u}(\mathbf{x}_s))_j + \int_{\partial\Omega} \mathbf{n}\cdot\hat{\Sigma}^j(\xi, \mathbf{x}_s)\cdot\mathbf{u}(\xi)\,dS_\xi,$$

$$\lim_{\mathbf{x}\in\Omega^c\to\mathbf{x}_s}\left\{\int_{\partial\Omega} \mathbf{n}\cdot\hat{\Sigma}^j(\xi, \mathbf{x})\cdot\mathbf{u}(\xi)\,dS_\xi\right\} = -\tfrac{1}{2}(\mathbf{u}(\mathbf{x}_s))_j + \int_{\partial\Omega} \mathbf{n}\cdot\hat{\Sigma}^j(\xi, \mathbf{x}_s)\cdot\mathbf{u}(\xi)\,dS_\xi, \ \mathbf{x}_s\in\partial\Omega. \tag{13}$$

Here $\Omega^c = \mathbf{R}^3/(\Omega\cup\partial\Omega)$ is the exterior to Ω and its boundary $\partial\Omega$. Thus at the boundary equation (12) may be written as

$$-\tfrac{1}{2}(\mathbf{u}(\mathbf{x}_s))_j = \int_{\partial\Omega} (\mathbf{n}\cdot\mathbf{T}(\xi)\cdot\hat{\mathbf{v}}^j(\xi, \mathbf{x}_s) - \mathbf{n}\cdot\hat{\Sigma}^j(\xi, \mathbf{x}_s)\cdot\mathbf{u}(\xi))\,dS_\xi, \quad \mathbf{x}_s\in\partial\Omega. \tag{14}$$

Note that the problem has not actually been solved but instead recast as a system of integral equations. The normal tractions $\mathbf{f}$ are not known at the boundaries. The value of this boundary integral reformulation lies in the fact that knowledge of the boundary *velocity* (via boundary conditions) then allows direct calculation of the normal tractions via (14). The formulation (14) was used by Youngren and Acrivos[8] to calculate the drag forces on solid particles in an unbounded domain. In that case Ω corresponds to the unbounded fluid and $\partial\Omega$ to the surface of the particle.

However, when this 'standard' formulation is applied to the current problem, depicted in Figure 1, then necessarily $\partial\Omega = S_P + \mathbf{P}$. In this case the normal tractions must be calculated both on the body surface and on the planar wall $\mathbf{P}$. Although the unknown normal tractions can be determined numerically, the planar wall must necessarily be truncated at a *finite* distance from the axis of symmetry, and the remaining portion of the wall discretized.

A more efficient path used in the following sections of this paper is to choose a fundamental solution, or more correctly a Green function, that includes the no-slip boundary condition at the wall. Thus instead of (11) we use the solution of the system

$$\delta(\mathbf{x}-\xi)\mathbf{e}_j = \nabla_\xi \mathbf{q}^j(\xi, \mathbf{x}) + \nabla_\xi^2 \mathbf{v}^j(\xi, \mathbf{x}), \quad 0 = \nabla_\xi\cdot\mathbf{v}^j(\xi, \mathbf{x}), \tag{15}$$

$$\mathbf{v}^j(\xi, \mathbf{x}) = 0, \quad \xi\in\mathbf{P}, \quad \mathbf{x}\in\mathbf{R}^3 \tag{16}$$

as the fundamental solution or Green function to be superposed via (6). The solution to this system is discussed by Blake[13] and stems from the work of Oseen.[14] It is

$$v_i^j = -\frac{1}{8\pi}\left\{\frac{\delta_{ij}}{r}+\frac{r_i r_j}{r^3}-\frac{\delta_{ij}}{R}-\frac{R_i R_j}{R^3}+2x_3\Delta_j\frac{\partial}{\partial R_j}\left[\frac{x_3 R_i}{R^3}-\frac{\delta_{i3}}{R}-\frac{R_i R_3}{R^3}\right]\right\}$$

$$= -\frac{1}{8\pi}\left\{\frac{\delta_{ij}}{r}+\frac{r_i r_j}{r^3}-\frac{\delta_{ij}}{R}-\frac{R_i R_j}{R^3}+2x_3\Delta_j\left[x_3\left(\frac{\delta_{ij}}{R^3}-\frac{3R_i R_j}{R^5}\right)+\frac{\delta_{i3}}{R^3}R_j\right.\right.$$

$$\left.\left.-\frac{1}{R^3}\left(\delta_{ij}R_3+R_i\delta_{3j}\right)+\frac{3R_i R_j R_3}{R^5}\right]\right\}, \tag{17}$$

$$q^j = \frac{1}{4\pi}\left[\frac{r_j}{r^3}-\frac{R_j}{R^3}-2x_3\Delta_j\left(\frac{\delta_{3j}}{R^3}-\frac{3R_j R_3}{R^5}\right)\right], \tag{18}$$

$$\Sigma_{ik}^j = \frac{3}{4\pi}\left\{\frac{r_i r_j r_k}{r^5}-\frac{R_i R_j R_k}{R^5}-2x_3\Delta_j\left[-\frac{x_3}{R^5}\delta_{ik}R_j\right.\right.$$

$$\left.\left.+\frac{\xi_3}{R^5}(R_i\delta_{jk}+\delta_{ij}R_k)+\frac{R_i\delta_{3j}R_k}{R^5}-\frac{5R_i R_j R_k\xi_3}{R^7}\right]\right\}, \tag{19}$$

where $\mathbf{r}=(\xi_1-x_1,\ \xi_2-x_2,\ \xi_3-x_3)^{\mathrm{T}}$, $\mathbf{R}=(\xi_1-x_1,\ \xi_2-x_2,\ \xi_3+x_3)^{\mathrm{T}}$, $r=[(\xi_1-x_1)^2+(\xi_2-x_2)^2+(\xi_3-x_3)^2]^{1/2}$, $R=[(\xi_1-x_1)^2+(\xi_2-x_2)^2+(\xi_3+x_3)^2]^{1/2}$ and $R_3=\xi_3+x_3$. The quantity Δ_j has the value $+1$ for $j=1, 2$ and -1 for $j=3$. Note that the Green function (17)–(19) consists of the fundamental solution (11) plus terms due to the presence of the wall. It corresponds to the velocity, pressure and stress fields for a point force in the fluid in the presence of a plane wall upon which the no-slip condition has already been applied. Given the geometry of Figure 1, the analogue of equation (12) for this Green function is

$$-(\mathbf{u}(\mathbf{x}))_j = \int_{S_P}(\mathbf{n}\cdot\mathbf{T}(\xi)\cdot\mathbf{v}^j(\xi,\mathbf{x})-\mathbf{n}\cdot\boldsymbol{\Sigma}^j(\xi,\mathbf{x})\cdot\mathbf{u}(\xi))\,dS_\xi, \quad \mathbf{x}\in\mathbf{D} \quad \text{for } j=1,2,3. \tag{20}$$

In this expression, $\mathbf{n}$ is the normal vector pointing inward to $\mathbf{D}_c$. Because of condition (16), the surface integration in (20) is over S_P and not $S_P+\mathbf{P}$ as would be the case if the fundamental solution (11) were used. The additional wall terms are well behaved for $\mathbf{x}\in S_P$. As a result, each term above involving the kernel $\mathbf{v}^j$ is continuous for $\mathbf{x}\in S_P$. The terms involving the kernel $\boldsymbol{\Sigma}^j$ suffer a jump across S_P, but this discontinuity stems directly from the $\mathbf{r}$ terms, i.e. the terms present in the fundamental solution (11). Thus the jump condition follows from equation (13) and is

$$\lim_{\mathbf{x}\in\mathbf{D}\to\mathbf{x}_s}\left\{\int_{S_P}\mathbf{n}\cdot\boldsymbol{\Sigma}^j(\xi,\mathbf{x})\cdot\mathbf{u}(\xi)\,dS_\xi\right\} = \tfrac{1}{2}(\mathbf{u}(\mathbf{x}_s))_j+\int_{S_P}\mathbf{n}\cdot\boldsymbol{\Sigma}^j(\xi,\mathbf{x}_s)\cdot\mathbf{u}(\xi)\,dS_\xi,$$

$$\lim_{\mathbf{x}\in\mathbf{D}_c\to\mathbf{x}_s}\left\{\int_{S_P}\mathbf{n}\cdot\boldsymbol{\Sigma}^j(\xi,\mathbf{x})\cdot\mathbf{u}(\xi)\,dS_\xi\right\} = -\tfrac{1}{2}(\mathbf{u}(\mathbf{x}_s))_j+\int_{S_P}\mathbf{n}\cdot\boldsymbol{\Sigma}^j(\xi,\mathbf{x}_s)\cdot\mathbf{u}(\xi)\,dS_\xi, \quad \mathbf{x}_s\in S_P. \tag{21}$$

Thus in terms of the Green function (17)–(19) the system to be solved is

$$-\tfrac{1}{2}(\mathbf{u}_s(\mathbf{x}_s))_j = -\int_{S_P}\boldsymbol{\Sigma}^j(\xi,\mathbf{x}_s)\cdot\mathbf{u}_s(\xi)\cdot\mathbf{n}\,dS_\xi+\int_{S_P}\mathbf{v}^j(\xi,\mathbf{x}_s)\cdot\mathbf{f}(\xi)\,dS_P. \quad \mathbf{x}_s\in S_P. \tag{22}$$

This is the primary result of this section. Equation (22) provides a relationship between the unknown tractions $\mathbf{f}$ on the particle surface and the particle velocity for arbitrary particle–wall geometries and base flows.

Formulation for particle translation in an otherwise quiescent fluid

For the case in which the particle translates in an otherwise quiescent fluid, the result (22) can be simplified further. In this case $\mathbf{u}(\mathbf{x}_s) = \mathbf{u}_s$ is a constant for $\mathbf{x}_s \in S_P$. Modifying the arguments of Ladyzhenskaya,[9] it can be shown that for a constant vector C,

$$\int_{S_P} \mathbf{n}\cdot\boldsymbol{\Sigma}^j(\boldsymbol{\xi}, \mathbf{x})\cdot\mathbf{C}\,dS_\xi = \begin{cases} 0, & \mathbf{x}\in\mathbf{D}, \\ -\frac{1}{2}\mathbf{C}_j, & \mathbf{x}\in S_P, \\ -\mathbf{C}_j, & \mathbf{x}\in\mathbf{D}_c. \end{cases}$$

Using this fact, we obtain a linear integral equation of the first kind for $\mathbf{f}$:

$$-(\mathbf{u}_s)_j = \int_{S_P} \mathbf{v}^j(\boldsymbol{\xi}, \mathbf{x}_s)\cdot\mathbf{f}(\boldsymbol{\xi})\,dS_\xi, \quad \mathbf{x}_s\in S_P. \tag{23}$$

For the case of axisymmetric motion, i.e. $\mathbf{u}_s = -\mathbf{e}_z$ with the particle oriented such that it possesses axisymmetry about the z-axis, these equations simplify further, Here the particle is a body of revolution with z-axis being the axis of revolution. For convenience, a cylindrical coordinate system is employed with $\rho = \sqrt{(x^2 + y^2)}$. There are several ways in which the particle surface may be represented. The simplest (used by Youngren and Acrivos[8]) is to define the particle surface as $(\rho(z), z)$ for $\theta\in[0, 2\pi)$, the functional dependence of ρ on z being given. This representation implicitly limits the types of surfaces which can be considered to those for which ρ is a single-valued function of z. An equally simple but more general representation, which avoids this potential problem, is to parametrically define the surface as $(\rho(s), z(s))$ for $\theta\in[0, 2\pi)$, where s is a parametric independent variable. This was the approach taken here.

The dependence of the integrands on θ in this system is known explicitly, and integration with respect to this variable may be performed. Although the resulting integration yields quite complex expressions, the net result is the reduction of the integration domain from two dimensions to one. The resulting equation for the unknown surface stress components f_ρ and f_z is

$$\begin{pmatrix} 0 \\ -1 \end{pmatrix} = -\int_{s_0}^{s_f} \mathbf{Q}(\boldsymbol{\xi}(s), \mathbf{x}_s)\cdot\begin{pmatrix} f_\rho \\ f_z \end{pmatrix}\rho(s)(\dot\rho^2(s) + \dot z^2(s))^{1/2}\,ds, \quad \mathbf{x}_s\in S_P, \tag{24}$$

where $\dot\rho(s)$ and $\dot z(s)$ are the derivatives of ρ and z with respect to s, and

$$\begin{aligned}
-8\pi Q_{11} &= C_1^{01} - \hat C_1^{01} + \rho\rho_o(C_3^{02} - \hat C_3^{02}) + (\rho^2 + \rho_o^2)(C_3^{01} - \hat C_3^{01}) \\
&\quad + \rho\rho_o(C_3^{00} - \hat C_3^{00}) - 2z_o z[\hat C_3^{01} - 3\{(\rho^2 + \rho_o^2)\hat C_5^{01} + \rho\rho_o(\hat C_5^{02} + \hat C_5^{00})\}], \\
8\pi Q_{12} &= \rho(r_3 C_3^{01} - R_3\hat C_3^{01}) + \rho_o(r_3 C_3^{00} - R_3\hat C_3^{00}) \\
&\quad + 2z_o[\rho\hat C_3^{01} + \rho_o\hat C_3^{00} + 3zR_3(\rho\hat C_5^{01} + \rho_o\hat C_5^{00})], \\
8\pi Q_{21} &= \rho_o(r_3 C_3^{01} - R_3\hat C_3^{01}) + \rho(r_3 C_3^{00} - R_3\hat C_3^{00}) \\
&\quad + 2z_o[\rho_o\hat C_3^{01} + \rho\hat C_3^{00} - 3zR_3(\rho_o\hat C_5^{01} + \rho\hat C_5^{00})], \\
-8\pi Q_{22} &= C_1^{00} - \hat C_1^{00} + r_3^2 C_3^{00} - R_3^2\hat C_3^{00} + 2z_o z(\hat C_3^{00} - 3R_3^2\hat C_5^{00}).
\end{aligned}$$

Here the integration variable $\boldsymbol{\xi}$ has been written as (ρ, z) and (ρ_o, z_o) corresponds to $\mathbf{x}_s$, the fixed point in the integration. Also, $r_3 = z - z_o$ and $R_3 = z + z_o$. The expressions C_p^{nm} and

$\hat{C}_p^{nm}$ are defined as

$$C_p^{nm} \equiv \frac{2}{\gamma^{p/2}} \int_0^{\pi} \frac{\sin^n 2x \cos^m 2x}{[1 - k^2 \sin^2 x]^{p/2}} \, dx \tag{25}$$

and

$$\hat{C}_p^{nm} \equiv \frac{2}{\gamma_R^{p/2}} \int_0^{\pi} \frac{\sin^n 2x \cos^m 2x}{[1 - k_R^2 \sin^2 x]^{p/2}} \, dx, \tag{26}$$

where

$$\gamma = (\rho + \rho_o)^2 + r_3^2, \qquad k^2 = 4\rho\rho_o/\gamma$$

and

$$\gamma_R = (\rho + \rho_o)^2 + R_3^2, \qquad k_R^2 = 4\rho\rho_o/\gamma_R.$$

Expressions (25)–(26) for C_p^{nm} and $\hat{C}_p^{nm}$ have been analytically evaluated, and the results of the integrations are given in the Appendix.

Implementation

System (24) may be discretized and solved numerically. The approach taken here is that used by Youngren and Acrivos,[8] i.e. the method of Krylov–Bogoliubov.[15] Specifically, the particle arc, which is given by $(\rho(s), z(s))$, for $s \in [s_o, s_f]$, is divided into N elements. This is accomplished by dividing the interval $[s_o, s_f]$ into subintervals Δs_j with centres s_j $(j = 1, \ldots, N)$. Each parametric value s_j corresponds to a point on the arc $\mathbf{x}_j = (\rho(s_j), z(s_j))$, and each Δs_j corresponds to a segment or element of the arc. The elements are assumed to be sufficiently small that the local normal tractions f_ρ and f_z may be assumed constant within each element. The resulting discretized system is

$$\begin{pmatrix} 0 \\ -1 \end{pmatrix} \simeq -\sum_{j=1}^{N} \left\{ \left[\int_{\Delta s_j} \mathbf{Q}(\boldsymbol{\xi}(s), \mathbf{x}_i) \, \rho(s) (\dot{\rho}^2(s) + \dot{z}^2(s))^{1/2} \, ds \right] \cdot \begin{pmatrix} f_\rho(\mathbf{x}_j) \\ f_z(\mathbf{x}_j) \end{pmatrix} \right\}, \quad 1 \leqslant i \leqslant N. \tag{27}$$

This is a linear system of $2N$ equations in the $2N$ unknowns $f_\rho(\mathbf{x}_j)$, $f_z(\mathbf{x}_j)$, where $1 \leqslant j \leqslant N$. Each coefficient

$$\left[\int_{\Delta s_j} \mathbf{Q}(\boldsymbol{\xi}(s), \mathbf{x}_i) \, \rho(s) (\dot{\rho}^2(s) + \dot{z}^2(s))^{1/2} \, ds \right] \tag{28}$$

for $j \neq i$ was evaluated by Gaussian quadrature. When $j = i$ and $s = s_i$ then $\boldsymbol{\xi}(s) = \mathbf{x}_i$, and the function $\mathbf{Q}$ becomes unbounded. In this case the region Δs_j is subdivided into three smaller regions, one of which is centred at the singular point s_j and is $\Delta_j^{\text{sing}} = [s_j - \varepsilon/2, s_j + \varepsilon/2]$. The constant ε is assumed small enough that over Δ_j^{sing} the arc may be accurately approximated by the tangent line through the point $\mathbf{x}_j$. Following Lee and Leal,[11] the singular contribution to equation (27) from over the interval Δ_j^{sing} can be approximated analytically. The details of the singular contribution are given in the Appendix. In the remaining two portions of the singular element Δs_j, accurate Rhomberg integration was performed. The linear system was solved using a standard matrix inverter.

NUMERICAL RESULTS

Axisymmetric flow calculations were performed on the class of ellipsoidal particles given by (Figure 2(a))

$$\rho^2/a^2 + z^2/b^2 = 1,$$

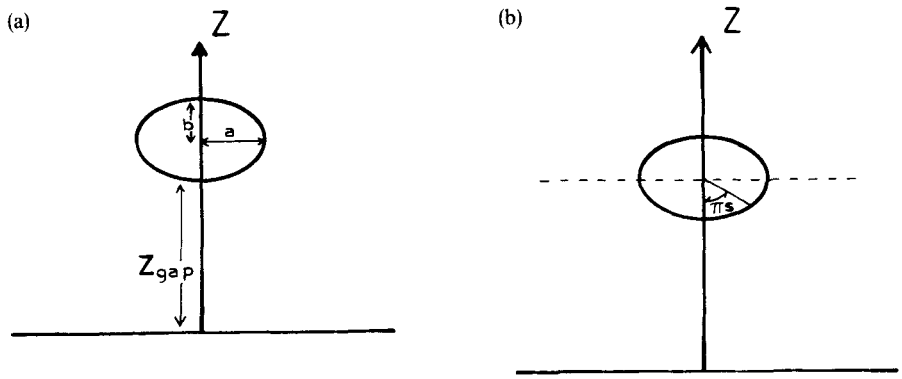

Figure 2. (a) Ellipsoid geometrical parameters. (b) The parametrization variable s

or equivalently, written in parametric form,

$$z = z_{gap} + b\left[\sin\left(\pi s - \frac{\pi}{2}\right) + 1\right], \quad \rho = a\cos\left(\pi s - \frac{\pi}{2}\right), \quad s \in [0, 1].$$

The parameters a, b and z_{gap} have been made dimensionless with respect to the length l, which is the radius of a sphere of equivalent volume. This non-dimensionalization provides a relationship between a and b. In fact, if $\alpha = b/a$ then $b = \alpha^{2/3}$ and $a = \alpha^{-1/3}$. Thus α and z_{gap}, the minimum particle-to-wall distance, are the only geometric variables in the system. The case of a sphere is recovered by setting $\alpha = 1$. The parametric variable s was chosen for simplicity, and in fact πs corresponds to the angle shown in Figure 2(b). A non-optimal strategy of constant element width Δs was employed. In all cases the particle drag was normalized with respect to the theoretical values for an unbounded fluid.[16] The normalized drag force is denoted by λ.

Sphere near a plane wall

For the special case of a sphere, 'exact' values of λ are given by[1]

$$\lambda = \frac{4}{3}\sinh(\omega)\sum_{n=1}^{\infty}\frac{n(n+1)}{(2n-1)(2n+3)}\left\{\frac{2\sinh[(2n+1)\omega] + (2n+1)\sinh(2\omega)}{4\sinh^2[(n+\frac{1}{2})\omega] - (2n+1)^2\sinh^2(\omega)} - 1\right\}, \tag{29}$$

where

$$\omega = \ln[z_{gap} + 1 + \sqrt{(z_{gap}^2 + 2z_{gap})}].$$

Table I lists the results from expression (29) as well as numerical results obtained here with 10, 20, 30 and 40 elements on the surface of the sphere. Even for 10 elements, the numerical and theoretical results are in excellent agreement. For all values of z_{gap} in the range 100 to 0·25 the error is less than 0·5% for 10 elements, less than 0·09% for 20 elements, 0·05% for 30 elements and less than 0·03% for 40 elements. For smaller values of z_{gap} the accuracy deteriorates for all numbers of elements because the magnitudes of the local stresses and stress gradients increase dramatically on the wall side of the sphere as z_{gap} decreases. Large stress gradients lead to a breakdown of the constant-within-each-element assumption and so degrade numerical accuracy.

The evolution of the local surface stresses as the sphere approaches the wall is plotted in Figures 3(a) and 3(b) for the 40-element case. An increase in the number of elements in the small-z_{gap} case improves the overall accuracy. This is demonstrated by the fact that with 40

Table I. A comparison of numerical results using the wall Green function with the theoretical results of Brenner (equation (29)) for the case of a sphere. Results for number of elements, N, equal to 10, 20, 30 and 40 are shown

		$N = 10$		$N = 20$		$N = 30$		$N = 40$	
z_{gap}	λ (theoretical)	λ (numerical)	Error*	λ (numerical)	Error*	λ (numerical)	Error*	λ (numerical)	Error*
100	1·011263	1·01532	0·401	1·01222	0·095	1·01167	0·040	1·01148	0·021
75	1·015024	1·01910	0·402	1·01598	0·094	1·01543	0·040	1·01524	0·021
50	1·022553	1·02665	0·401	1·02352	0·095	1·02296	0·040	1·02277	0·021
25	1·045196	1·04937	0·399	1·04617	0·093	1·04560	0·039	1·0454	0·020
10	1·113503	1·11768	0·375	1·11428	0·067	1·11367	0·015	1·11347	−0·003
9	1·126194	1·13032	0·366	1·12688	0·061	1·12627	0·007	1·12606	−0·012
8	1·142068	1·14632	0·372	1·14283	0·067	1·14222	0·013	1·14201	−0·005
7	1·162491	1·16688	0·378	1·16334	0·073	1·16271	0·019	1·16249	−0·0001
6	1·189737	1·19428	0·382	1·19065	0·077	1·19001	0·023	1·18980	0·005
5	1·227889	1·23264	0·387	1·22889	0·082	1·22823	0·028	1·22800	0·009
4	1·285087	1·29008	0·389	1·28618	0·085	1·28548	0·031	1·28525	0·013
3	1·380204	1·38558	0·389	1·38140	0·087	1·38066	0·033	1·38041	0·015
2	1·569205	1·57532	0·390	1·57057	0·087	1·56974	0·034	1·56946	0·016
1	2·125536	2·13369	0·384	2·12730	0·083	2·12620	0·031	2·12584	0·014
0·75	2·489273	2·49864	0·376	2·49123	0·079	2·48998	0·028	2·48957	0·012
0·5	3·205390	3·21674	0·354	3·20751	0·066	3·20603	0·020	3·20558	0·006
0·25	5·305324	5·31976	0·272	5·30508	−0·005	5·30405	−0·024	5·30393	−0·026
0·10	11·459157	11·79521	2·93	11·40327	−0·488	11·41799	−0·359	11·42883	−0·265
0·05	21·585818	26·60858	23·3	21·56331	−0·104	21·29163	−1·36	21·34026	−1·14

* Error is defined as $100 \times [\lambda(\text{numerical}) - \lambda(\text{theoretical})]/\lambda(\text{theoretical})$.

elements and $z_{gap} = 0{\cdot}1$ the error in the normalized drag is 0·265%, as compared with 2·93% for 10 elements. In the closest case of $z_{gap} = 0{\cdot}05$ with 40 elements the error in drag is only 1·13%.

For the sake of comparison, sphere calculations were also performed using the classical boundary integral technique with the stokeslet fundamental solution. This entailed integration over the planar wall. The planar wall was discretized by truncating at a radial distance denoted by ρ_t and placing N_{wall} elements in the interval from $\rho = 0$ to ρ_t. N_{sphere} elements of constant Δs width were used on the sphere surface. On the wall, elements of constant as well as non-constant width $\Delta\rho$ were employed. The non-constant width elements were selected so that the $\Delta\rho$ was small near $\rho = 0$ and increasing in size to $\rho = \rho_t$.* The results are given in Tables II–V where the numerical values for various combinations of N_{wall}, N_{sphere} and ρ_t are compared with the exact solutions of Brenner. Although the accuracy obtained is quite good when the sphere is far from the wall for the majority of the cases considered, accuracy degrades rapidly as the sphere approaches the wall. As expected, when the sphere is near the wall the accuracy is best when the wall elements near $\rho = 0$ are smallest, since smaller elements are capable of resolving the large variation in wall

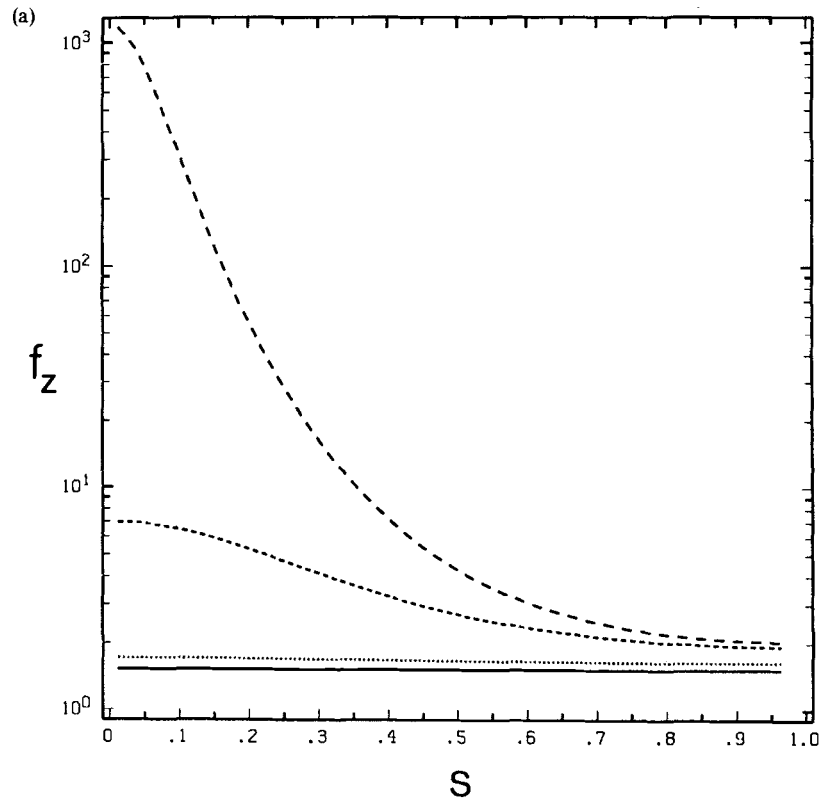

Figure 3. (a) Evolution of the z-component of the local surface tractions as z_{gap} decreases: ——, $z_{gap} = 100$, ····, $z_{gap} = 10$; - - -, $z_{gap} = 1$; – –, $z_{gap} = 0{\cdot}05$

* There are an infinite number of choices for such a non-constant distribution of elements. The current choice was made arbitrarily and for simplicity. If $\hat{\rho}_j = \rho_t[(j - 1/2)/N_{wall}]^2$ then the jth element is the interval $[(\hat{\rho}_{j-1} + \hat{\rho}_j)/2, (\hat{\rho}_{j+1} + \hat{\rho}_j)/2]$ for $j = 2, 3, \ldots, N_{wall} - 1$. The first interval is $[0, (\hat{\rho}_1 + \hat{\rho}_2)/2]$ and the last interval is $[(\hat{\rho}_{N_{wall}-1} + \hat{\rho}_{N_{wall}-2})/2, \rho_t]$. $z_j = 0$ for all intervals. This distribution corresponds approximately to a linear increase in the $\Delta\rho$ width moving outward along the wall.

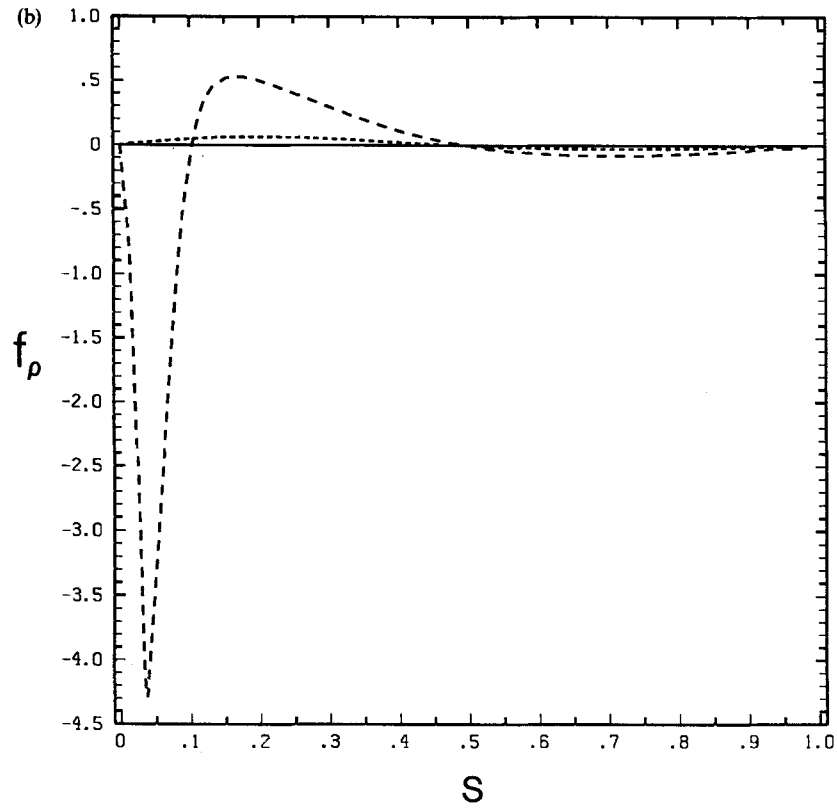

Figure 3. (b) Evolution of the ρ-component of the local surface tractions as z_{gap} decreases: ——, $z_{gap}=100$; · · ·, $z_{gap}=10$; - - -, $z_{gap}=1$; – –, $z_{gap}=0{\cdot}05$. Note that in (b) the $z_{gap}=100$ curve and the $z_{gap}=10$ curve are visually indistinguishable. In both (a) and (b) the arbitrary constant due to pressure has been chosen so that $f_\rho=0$ at $s=0{\cdot}5$

surface traction. Thus for both constant and non-constant width elements the best accuracy near the wall for a given N_{wall} occurs when ρ_t is smallest.

The stokelet and Green function methods are best compared on the basis of the total number of elements, N_{total}, where $N_{total} = N_{wall} + N_{sphere}$ for the stokeslet case and N_{total} is taken to be the number of elements, N, on the particle surface for the Green function method. Overall, for the same N_{total} the Green function results are far superior in accuracy to the stokeslet results. In particular, the Green function results for $N = N_{total} = 30$, with few exceptions, are more accurate than any of the stokeslet results for $N_{total} = 60$ ($N_{wall} = 30$, $N_{sphere} = 30$). It is anticipated that the accuracy of the stokeslet method may be improved by distributing more smaller-width elements near $\rho = 0$ on the wall. Nevertheless, such redistributions are *ad hoc* and of unlimited variety. Further, such redistribution of points on the sphere surface for both the Green function and stokeslet methods could also undoubtedly lead to increased accuracy. Employing the Green function entirely eliminates the need for *ad hoc* choices of *wall* element distributions and *wall* truncation distances. For the solid sphere problem Brenner's exact solution is known, and the dependence of the accuracy of the stokeslet method on the parameters N_{wall}, ρ_t and the distribution of elements can be determined. In any realistic problem the choice of these parameters may be difficult or unmotivated.

Table II. A comparison of numerical results generated using the stokeslet fundamental solution and $N_{sphere} = 6$, $N_{wall} = 6$ with the theoretical results of Brenner (equation (29)) for the case of a sphere: (a) constant width wall elements; (b) non-constant width wall elements

(a)

z_{gap}	λ (analytic)	λ ($\rho_t = 25$)	Error	λ ($\rho_t = 50$)	Error
100	1·011263	1·015590	0·428	1·018810	0·746
75	1·015024	1·018660	0·358	1·023150	0·801
50	1·022553	1·026260	0·363	1·032010	0·925
25	1·045196	1·052580	0·706	1·056430	1·07
10	1.113503	1·125140	1·05	1·125940	1·12
9	1·126194	1·138050	1·05	1·138890	1·13
8	1·142068	1·154130	1·06	1·154960	1·13
7	1·162491	1·174800	1·06	1·175150	1·09
6	1·189737	1·202420	1·07	1·200600	1·913
5	1·227889	1·241260	1·09	1·232290	0·358
4	1·285087	1·299680	1·14	1·269840	−1·19
3	1·380204	1·394650	1·05	1·308740	−5·18
2	1·569205	1·556630	−0·801	1·336160	−14.9
1	2·125536	1·790740	−15·8	1·331850	−37.3
0·75	2·489273	1·841520	−26·0	1·324160	−46·8
0·5	3·205390	1·875680	−41·5	1·314010	−59·0
0·25	5·305324	1·885720	−64·5	1·301850	−75·5
0·1	11·45916	1·878580	−83·6	1·294010	−88·7
0·05	21·58582	1·874220	−91·3	1·291440	−94·0

(b)

z_{gap}	λ (analytic)	λ ($\rho_t = 25$)	Error	λ ($\rho_t = 50$)	Error
100	1·011263	1·015480	0·417	1·018690	0·734
75	1·015024	1·018490	0·341	1·023010	0·787
50	1·022553	1·026000	0·337	1·031910	0·915
25	1·045196	1·052360	0·685	1·056490	1·08
10	1·113503	1·125430	1·071	1·126320	1·15
9	1·126194	1·138440	1·087	1·139300	1·16
8	1·142068	1·154660	1·103	1·155600	1·18
7	1·162491	1·175500	1·119	1·176710	1·22
6	1·189737	1·203290	1·139	1·205120	1.29
5	1·227889	1·242210	1·166	1·245240	1.41
4	1·285087	1·300720	1·216	1·305390	1·58
3	1·380204	1·399000	1·362	1·403730	1·70
2	1·569205	1·598540	1·869	1·596800	1·76
1	2·125536	2·185370	2·82	2·292810	7·87
0·75	2·489273	2·566520	3·10	2·937180	18·0
0·5	3·205390	3·403570	6·18	4·742860	48·0
0·25	5·305324	7·652900	44·2	13·30720	151
0.1	11·45916	30·20205	164	115·2971	906
0·05	21·5858	35·74634	61·0	—	—

Table III. A comparison of numerical results generated using the stokeslet fundamental solution and $N_{sphere} = 10$, $N_{wall} = 10$ with the theoretical results of Brenner (equation (29)) for the case of a sphere: (a) constant width wall elements; (b) non-constant width wall elements

(a)

z_{gap}	λ (analytic)	λ ($\rho_t = 25$)	Error	λ ($\rho_t = 50$)	Error
100	1·011263	1·008330	−0·290	1·011540	0·027
75	1·015024	1·011400	−0·357	1·015860	0·082
50	1·022553	1·018990	−0·348	1·024650	0·205
25	1·045196	1·045130	−0·006	1·048880	0·352
10	1·113503	1·117210	0·333	1·117560	0·364
9	1·126194	1·130050	0·342	1·130260	0·361
8	1·142068	1·146030	0·347	1·146180	0·360
7	1·162491	1·166540	0·348	1·166740	0·366
6	1·189737	1·193830	0·344	1·194300	0·386
5	1·227889	1·231980	0·333	1·233000	0·416
4	1·285087	1·289180	0·319	1·290090	0·389
3	1·380204	1·384720	0·327	1·377360	−0·206
2	1·569205	1·576370	0·457	1·505340	−4·07
1	2·125536	2·083520	−1·98	1·637900	−22·9
0·75	2·489273	2·320980	−6·76	1·654970	−33·5
0·5	3·205390	2·612240	−18·5	1·658980	−48·2
0·25	5·305324	2·937680	−44·6	1·647910	−68·9
0·1	11·45916	3·139810	−72·6	1·634120	−85·7
0·05	21·58582	3·208300	−85·1	1·628570	−92·5

(b)

z_{gap}	λ (analytic)	λ ($\rho_t = 25$)	Error	λ ($\rho_t = 50$)	Error
100	1·011263	1·008260	−0·297	1·011460	0·019
75	1·015024	1·011300	−0·367	1·015770	0·073
50	1·022553	1·018820	−0·365	1·024570	0·197
25	1·045196	1·044970	−0·022	1·048880	0·352
10	1·113503	1·117260	0·337	1·117840	0·389
9	1·126194	1·130130	0·350	1·130600	0·391
8	1·142068	1·146180	0·360	1·146570	0·394
7	1·162491	1·166760	0·367	1·167120	0·398
6	1·189737	1·194180	0·373	1·194560	0·405
5	1·227889	1·232540	0·379	1·233040	0·420
4	1·285087	1·290050	0·386	1·290850	0·448
3	1·380204	1·385750	0·402	1·387280	0·513
.2	1·569205	1·576420	0·460	1·580980	0·750
1	2·125536	2·142720	0·808	2·172760	2·22
0·75	2·489273	2·520320	1·25	2·563390	2·98
0·5	3·205390	3·294110	2·77	3·327460	3·81
0·25	5·305324	5·750570	8·39	6·182470	16·5
0·1	11·45916	13·27579	15·9	25·47089	122
0·05	21·58582	21·02722	−2·59	27·62877	28·0

Table IV. A comparison of numerical results generated using the stokeslet fundamental solution and $N_{sphere} = 20$, $N_{wall} = 20$ with the theoretical results of Brenner (equation (29)) for the case of a sphere: (a) constant width wall elements; (b) non-constant width wall elements

(a)

z_{gap}	λ (analytic)	λ ($\rho_t = 25$)	Error	λ ($\rho_t = 50$)	Error	λ ($\rho_t = 100$)	Error
100	1·011263	1·005340	−0·586	1·008550	−0·268	1·011310	0·005
75	1·015024	1·008420	−0·651	1·012870	−0·212	1·015470	0·044
50	1·022553	1·016020	−0·639	1·021630	−0·090	1·023340	0·077
25	1·045196	1·042100	−0·296	1·045780	0·056	1·046120	0·088
10	1·113503	1·113980	0·043	1·114390	0·080	1·114270	0·069
9	1·126194	1·126790	0·053	1·127060	0·077	1·126930	0·065
8	1·142068	1·142760	0·061	1·142900	0·073	1·142810	0·065
7	1·162491	1·163260	0·066	1·163270	0·067	1·163320	0·071
6	1·189737	1·190540	0·067	1·190430	0·058	1·190820	0·091
5	1·227889	1·228680	0·064	1·228440	0·045	1·229440	0·126
4	1·285087	1·285790	0·055	1·285470	0·030	1·286430	0·105
3	1·380204	1·380630	0·031	1·380790	0·042	1·373560	−0·481
2	1·569205	1·568760	−0·028	1·572100	0·184	1·501380	−4·32
1	2·125536	2·126090	0·026	2·078760	−2·20	1·633810	−23·1
0·75	2·489273	2·496450	0·288	2·316190	−6·95	1·650860	−33·7
0·5	3·205390	3·212790	0·231	2·607630	−18·6	1·654870	−48·4
0·25	5·305324	4·881460	−7·99	2·933810	−44·7	1·643760	−69·0
0·1	11·45916	7·284840	−36·4	3·136340	−72·6	1·629750	−85·8
0·05	21·58582	8·783280	−59·3	3·204850	−85·2	1·623890	−92·5

(b)

z_{gap}	λ (analytic)	λ ($\rho_t = 25$)	Error	λ ($\rho_t = 50$)	Error	λ ($\rho_t = 100$)	Error
100	1·011263	1·005310	−0·589	1·008510	−0·272	1·011290	0·026
75	1·015024	1·008370	−0·656	1·012820	−0·217	1.015460	0·043
50	1·022553	1·015940	−0·647	1·021590	−0·094	1·023330	0·076
25	1·045196	1·042010	−0·305	1·045780	0·056	1·046140	0·090
10	1·113503	1.113970	0·042	1·114490	0·089	1·114490	0·089
9	1·126194	1·126800	0·054	1·127190	0·088	1·127190	0·088
8	1·142068	1·142780	0·062	1·143080	0·089	1·143080	0·089
7	1·162491	1·163300	0·070	1·163520	0·089	1·163530	0·089
6	1·189737	1·190620	0·074	1·190790	0·089	1·190810	0·090
5	1·227889	1·228820	0·076	1·228980	0·089	1·229030	0·093
4	1·285087	1·286060	0·076	1·286240	0·090	1·286370	0·100
3	1·380204	1·381200	0·072	1·381500	0·094	1·381850	0·119
2	1·569205	1·570230	0·065	1·570960	0·112	1·572140	0·187
1	2·125536	2·126880	0·063	2·130670	0·242	2·137710	0·573
0·75	2·489273	2·491240	0·079	2·498970	0·390	2·515210	1·04
0·5	3·205390	3·210330	0·154	3·231620	0·818	3·290070	2·64
0·25	5·305324	5·344480	0·738	5·463540	2·98	5·757460	8·52
0·1	11·45916	12·07906	5·41	13·84710	20·8	15·27464	33·3
0·05	21·58582	24·72773	14·6	30·57144	41·6	36·88208	70·9

Table V. A comparison of numerical results generated using the stokeslet fundamental solution and $N_{sphere} = 30$, $N_{wall} = 30$ with the theoretical results of Brenner (equation (29)) for the case of a sphere: (a) constant width wall elements; (b) non-constant width wall elements

(a)

z_{gap}	λ (analytic)	λ ($\rho_t = 25$)	Error	λ ($\rho_t = 50$)	Error	λ ($\rho_t = 100$)	Error
100	1·011263	1·004810	−0·638	1·008020	−0·321	1·010770	−0·049
75	1·015024	1·007900	−0·702	1·012330	−0·265	1·014930	−0·009
50	1·022553	1·015500	−0·690	1·021090	−0·143	1·022790	0·023
25	1·045196	1·041570	−0·347	1·045230	0·003	1·045570	0·036
10	1·113503	1·113410	−0·008	1·113840	0·030	1·113760	0·023
9	1·126194	1·126220	0·002	1·126520	0·029	1·126410	0·019
8	1·142068	1·142190	0·011	1·142380	0·027	1·142230	0·014
7	1·162491	1·162690	0·017	1·162770	0·024	1·162580	0·008
6	1·189737	1·189970	0·020	1·189960	0·019	1·189740	0·0003
5	1·227889	1·228130	0·020	1·228010	0·010	1·227860	−0·002
4	1·285087	1·285290	0·016	1·285000	−0·007	1·285370	0·022
3	1·380204	1·380240	0·003	1·379710	−0·036	1·381670	0·106
2	1·569205	1·568640	−0·036	1·568270	−0·060	1·566050	−0·201
1	2·125536	2·121690	−0·181	2·131500	0·281	1·935660	−8·93
0·75	2·489273	2·483940	−0·214	2·487960	−0·053	2·054850	−17·5
0.5	3·205390	3·207130	0·054	3·089850	−3·60	2·166220	−32·4
0·25	5·305324	5·347030	0·786	4·141040	−21·9	2·250720	−57·6
0·1	11·45916	10·288800	−10·2	5·206130	−54·6	2·280410	−80·1
0·05	21·58582	14.86634	−31·1	5·719160	−73·5	2·285870	−89·4

(b)

z_{gap}	λ (analytic)	λ ($\rho_t = 25$)	Error	λ ($\rho_t = 50$)	Error	λ ($\rho_t = 100$)	Error
100	1·011263	1·004790	−0.640	1·007990	−0·324	1·010750	−0·051
75	1·015024	1·007860	−0·706	1·012300	−0·268	1·014920	−0·010
50	1·022553	1·015440	−0·696	1·021060	−0·146	1·022780	0·022
25	1·045196	1·041510	−0·353	1·045220	0·002	1·045580	0·037
10	1·113503	1·113400	−0·009	1·113880	0·034	1·113890	0·035
9	1·126194	1·126220	0·002	1·126570	0·033	1·126580	0·034
8	1·142068	1·142200	0·012	1·142450	0·033	1·142460	0·034
7	1·162491	1·162700	0·018	1·162870	0·033	1·162880	0·033
6	1·189737	1·190010	0·023	1·190110	0·031	1·190120	0·032
5	1·227889	1·228200	0·025	1·228260	0·030	1·228270	0·031
4	1·285087	1·285420	0·026	1·285440	0·027	1·285480	0·031
3	1·380204	1·380520	0·023	1·380540	0·024	1·380640	0·032
2	1·569205	1·569440	0·015	1·569500	0·019	1·569850	0·041
1	2·125536	2·125380	−0·007	2·125960	0·020	2·128290	0·130
0·75	2·489273	2·488790	−0·019	2·490180	0·036	2·495210	0·238
0·5	3·205390	3·204310	−0·034	3·208820	0·107	3·223820	0·575
0·25	5·305324	5·305440	0·002	5·339160	0·638	5·437470	2·49
0·1	11·45916	11·56424	0·917	12·03615	5·04	13·49018	17·7
0.05	21·58582	22·63316	4·85	25.79175	19·5	32·16383	49·0

Figure 4 compares the computational time for the Green function and the stokeslet method as a function of N_{total}. When N_{total} is small the Green function method is approximately $1\frac{1}{2}$ times slower than the stokeslet method. The longer computational time of the Green function method for the same N_{total} is a direct consequence of the increased complexity of computing the Green function kernels compared with the stokeslet kernels. For larger N_{total} the time required to invert either the stokeslet or Green function linear systems for the same N_{total} (which is approximately the same since both systems are $2N_{total} \times 2N_{total}$ in size) becomes more important and the *ratio* of computational times tends toward unity. Note, however, that for comparable accuracy the Green function method requires less than half the total number of elements that the stokeslet method requires. Thus for a given level of accuracy the Green function method is actually substantially faster than the stokeslet method. All computations were performed on a Sun 3/160 workstation with a floating point accelerator. Absolute computational times were of the order of minutes (for instance, stokeslet method calculations with $N_{total} = 60$ took approximately 240 CPU seconds, $N_{total} = 40$ took 100 CPU seconds, $N_{total} = 20$ took 25 CPU seconds and $N_{total} = 12$ took 10 CPU seconds).

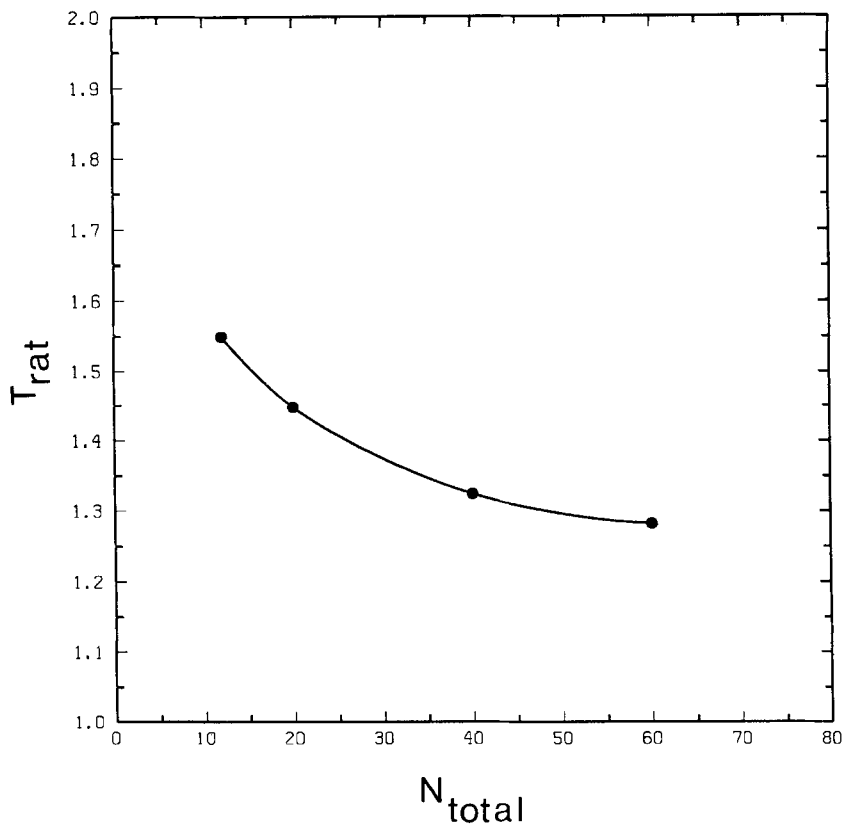

Figure 4. Comparison of computational time between the wall Green function technique and the stokeslet fundamental solution technique. T_{rat}, representing the ratio of computational times (Green method)/(stokeslet method), is plotted against N_{total}

Ellipsoids near a plane wall

Calculations were carried out for ellipsoids with axis ratios α of 0·0625, 0·125, 0·25, 0·5, 2, 4, 8 and 16. The parameter z_{gap} ranged from 0·05 to 100. Computations were terminated for small z_{gap} when calculated local stresses grew large and differed significantly in neighbouring elements (this generally occurred when the computed value of λ was of the order of several hundred).

Brenner[3] developed an asymptotic theory for the case when an arbitrarily shaped particle is in motion far from the wall. More specifically, if R_{eq} is the equivalent radius of the particle (defined such that $6\pi\mu U R_{eq}$ is the force exerted on the particle when falling with velocity U in the absence of the wall), then Brenner's asymptotic theory is valid for $z_c \overset{def}{=} z_{centre}/R_{eq} \gg 1$, where z_{centre} is the dimensional z-axis distance to the centre of the particle. This asymptotic theory predicts an expression of the form

$$\lambda = \frac{1}{1 - 9/8z_c + O(z_c^{-3})}. \tag{30}$$

Note that $z_c = (z_{gap} + \alpha^{2/3})(l/R_{eq})$, and for ellipsoidal particles R_{eq} is derived from the general expressions[16]

$$\frac{R_{eq}}{l} = \frac{8}{3(\alpha^{4/3}\kappa_0 + \beta_0)},$$

where

$$\kappa_0 = \frac{\beta_0\alpha^{2/3} - 2}{\alpha^2 - 1},$$

$$\beta_0 = \frac{\alpha^{1/3}}{\sqrt{(\alpha^2 - 1)}} \ln\left(\frac{\alpha + \sqrt{(\alpha^2 - 1)}}{\alpha - \sqrt{(\alpha^2 - 1)}}\right) \quad \text{for } \alpha^2 - 1 > 0,$$

$$\beta_0 = \frac{2\alpha^{1/3}}{\sqrt{(1 - \alpha^2)}}\left[\frac{\pi}{2} - \tan^{-1}\left(\frac{\alpha}{\sqrt{(1 - \alpha^2)}}\right)\right] \quad \text{for } \alpha^2 - 1 < 0.$$

Numerical results for the ellipsoid and sphere cases are compared with the large-z_c theory in Figures 5(a)–13(a). The most remarkable observation from these comparisons with the large-z_c theory is that the numerical results agree quantitatively with the large-z_c theory for values of z_c as small as 5, while *qualitative* agreement extends to even lower values of z_c, including the sharp upturn in λ for $z_c = 9/8$. However, it is clear that the far-field results cannot literally capture the singularity in λ and other detailed behaviour for very small z_{gap} (or z_c). For this purpose a more appropriate asymptotic analysis is via lubrication theory for flow in a thin film.

Using classical lubrication assumptions, Cox[6] developed an asymptotic theory which is valid for the case in which $z_{lub} \overset{def}{=} bz_{gap}/a^2 = z_{gap}\alpha^{4/3} \ll 1$. This theory predicts

$$\lambda = \frac{1}{\alpha^{4/3}(R_{eq}/l)z_{lub}} + O(\ln(z_{lub})). \tag{31}$$

Explicit in Cox's lubrication theory is the assumption that as $z_{lub} \to 0$ the approaching surfaces come together in *single-point* contact. Thus Cox's theory is not valid for the case of a disc approaching a planar wall with the face of the disc parallel to the wall. In fact, the case of a disc of radius R approaching a planar wall in this manner was analysed by Reynolds[7] who predicted

$$\lambda = \frac{R^4}{4R_{eq}z_{gap}^3}, \tag{32}$$

where $\hat{z}_{gap}$ is the dimensional gap distance. Notice that as $\hat{z}_{gap} \to 0$ equation (31) predicts λ increasing effectively as $1/\hat{z}_{gap}$, while equation (32) predicts $1/\hat{z}_{gap}^3$. Necessarily, when single-point contact will occur (as in all ellipsoid cases considered in this paper) then equation (31) predicts the correct limiting behaviour for sufficiently small $\hat{z}_{gap}$. Nevertheless, ellipsoids with sufficiently small values of α resemble discs with radii $R = bl$, and we may thus expect Reynolds' result, equation (32), to provide a reasonable approximation for some *intermediate* $\hat{z}_{gap}$ distances and sufficiently small values of α. For these ellipsoid cases equation (32) may be written as

$$\lambda = \frac{\alpha^{8/3}}{4(R_{eq}/l)z_{lub}^3}. \tag{33}$$

Numerical results for small z_{lub} values are plotted in Figures 5(b)–13(b) together with the asymptotic formula (31) and, where relevant, (33). For the case $\alpha = 1$ we also show Brenner's analytic theory for a sphere (equation (29)).

The results for $\alpha = 1$, 2 and 4 clearly approach the lubrication asymptote. On the other hand, for $\alpha = 8$ and 16 we were not able to capture the approach to asymptotic behaviour because computations were terminated for $z_{gap} = 0{\cdot}05$, and in these cases this corresponds to z_{lub} values well outside the range of validity of Cox's lubrication theory.

The numerical results for $\alpha < 1$ demonstrate the transition between Reynolds' result for the disc, (33), and the lubrication theory, (31), at 'intermediate' values of z_{lub} for small α. In particular,

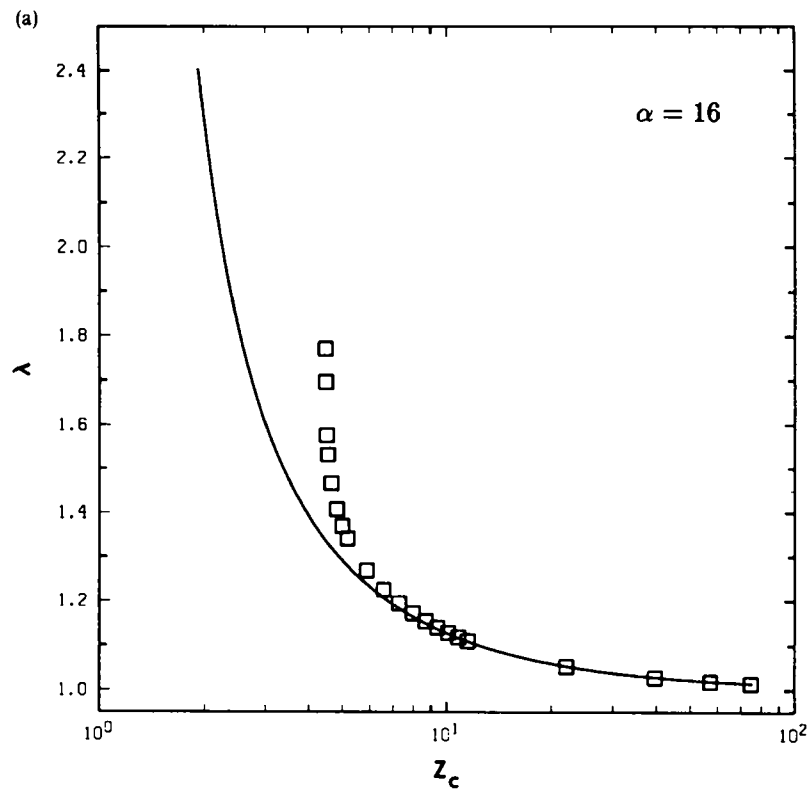

Figure 5. (a) Large-z_c results: □, numerical results for $\alpha = 16$ with 40 elements; ——, asymptotic predictions as given by equation (30)

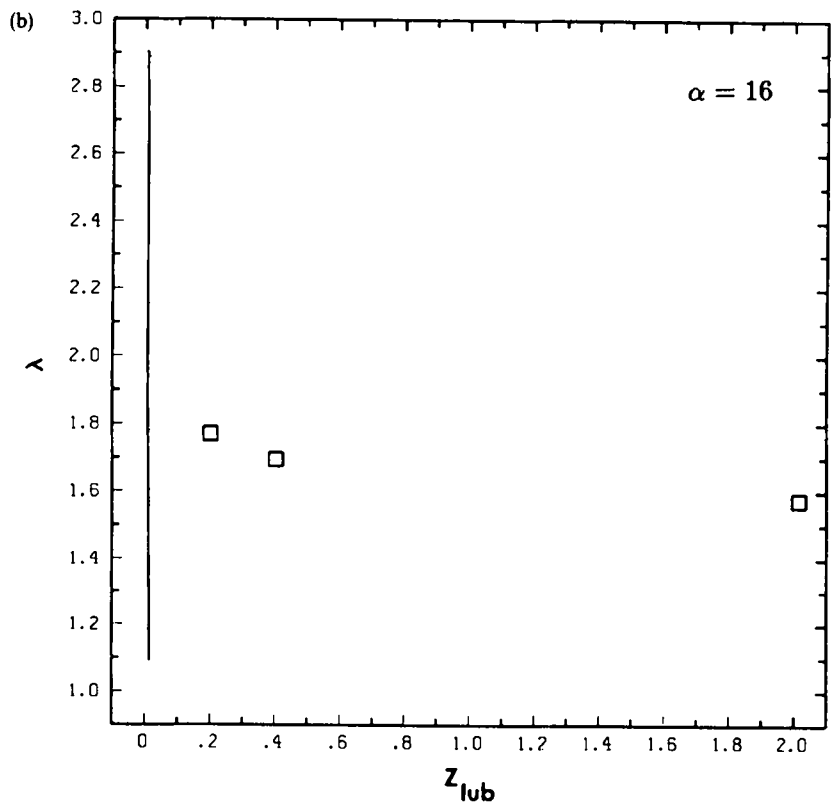

Figure 5. (b) Small-z_{lub} results: □, numerical results for $\alpha = 16$ with 40 elements; ——, Cox's lubrication theory as given by equation (31)

as α decreases from 0·5 to 0·0625 we see that the numerical results agree closely with (33) over a significant range of z_{lub} before (presumably) reverting to the lubrication asymptote for even smaller values of z_{lub}.

It should be noted, in all of the comparisons between our results and Cox's lubrication theory, that the latter is based on the implicit assumption that there exist extremely localized regions of high stresses and stress gradients near the point of smallest gap. Because of resolution difficulties, the current numerics break down when localized high stresses and stress gradients occur. Despite this fact, the numerics are able to provide information indicating trends, asymptotes and approximate regions of validity of Cox's lubrication theory. In particular, the numerics clearly indicate that Reynolds' lubrication theory is a better approximation than Cox's theory for small-α cases (0·125 and 0·0625 in particular) and intermediate z_{lub} values.

CONCLUSIONS

The wall Green function formulation of the boundary integral method for low-Reynolds-number flow was carefully tested against the analytic results of Brenner for the translation of a solid sphere toward a plane wall, and was found to yield highly accurate results up to

dimensionless gaps of 0·05. When compared to the boundary integral formulation using the stokeslet fundamental solution, the Green function formulation was found to be more accurate for the same total number of elements. In fact, the Green function method required approximately half the number of elements that the stokeslet method required to maintain the same level of accuracy. Although, the Green function formulation was slower computationally for the same N_{total}, the requirement of less elements to maintain the same level of accuracy easily compensates timewise for this disadvantage. The solid ellipsoid results compared extremely well with the far-field asymptotic results of Brenner for distances as small as $z_c = 5$. The current numerics as well as Brenner's analytic theory for a sphere (equation (29)) indicate an upper bound of $z_{lub} = 0{\cdot}05$ for the range of predictive validity of Cox's lubrication theory for the particle geometries considered here. Although as $z_{lub} \to 0$ Cox's lubrication theory necessarily predicts the correct limiting behaviour of λ, for the near-disc-like ellipsoids having α values of 0·25, 0·125 and 0·0625, the numerics indicate that Reynolds' lubrication theory for a disc is a more accurate approximation for intermediate z_{lub} values in the range $0{\cdot}05 < z_{lub} < 0{\cdot}1$.

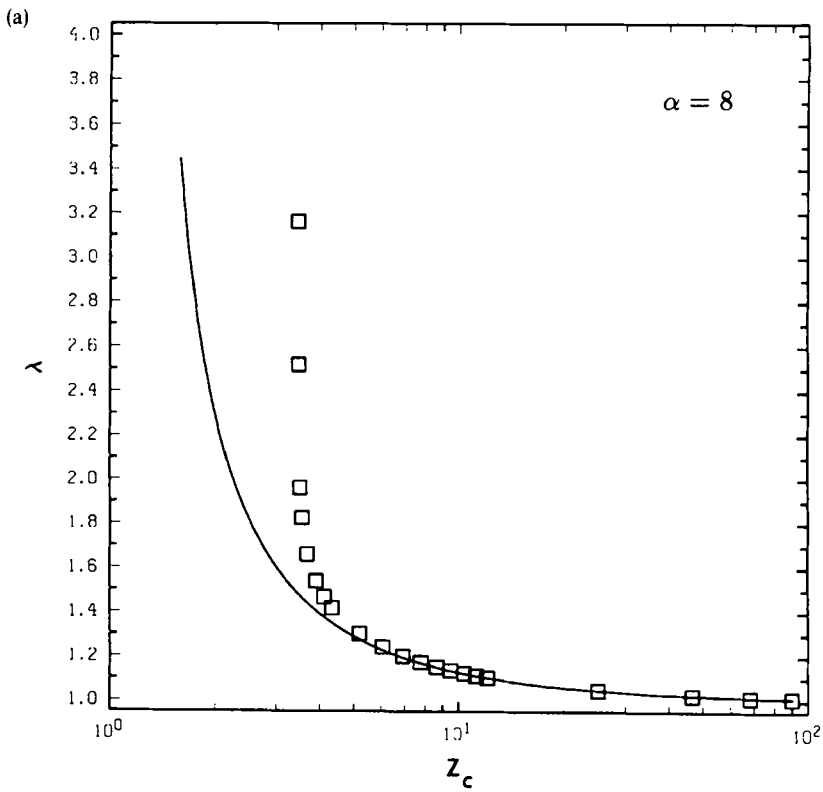

Figure 6. (a) Large-z_c results: □, numerical results for $\alpha = 8$ with 40 elements; —·—, the asymptotic predictions as given by equation (30)

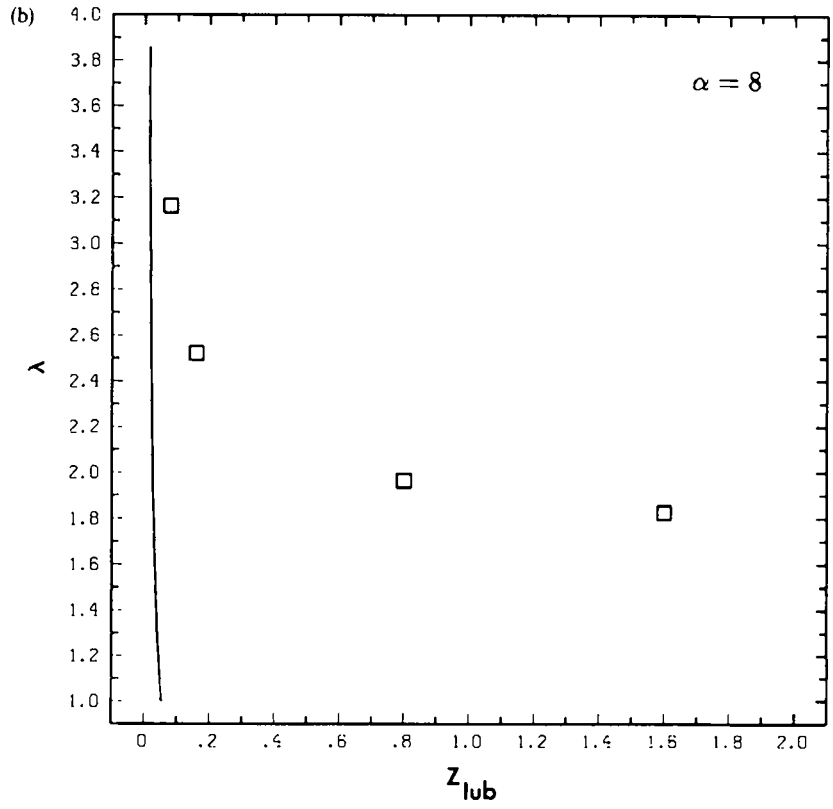

Figure 6. (b) Small-z_{lub} results: □, numerical results for $\alpha = 8$ with 40 elements; ——, Cox's lubrication theory as given by equation (31)

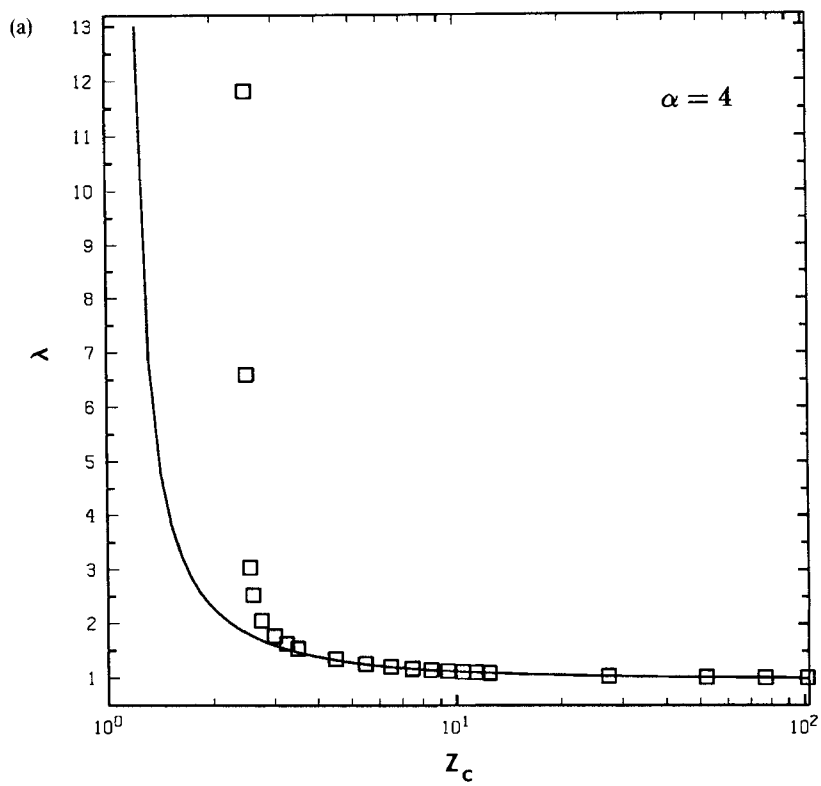

Figure 7. (a) Large-z_c results: □, numerical results for $\alpha = 4$ with 40 elements; ——, asymptotic predictions as given by equation (30)

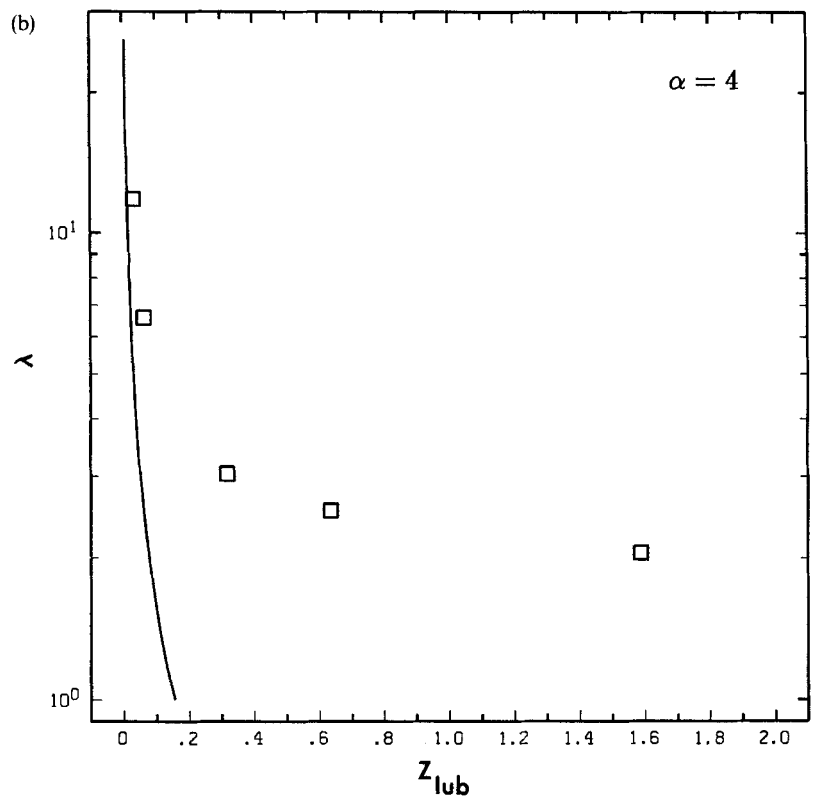

Figure 7. (b) Small-z_{lub} results: □, numerical results for $\alpha = 4$ with 40 elements; ——, Cox's lubrication theory as given by equation (31)

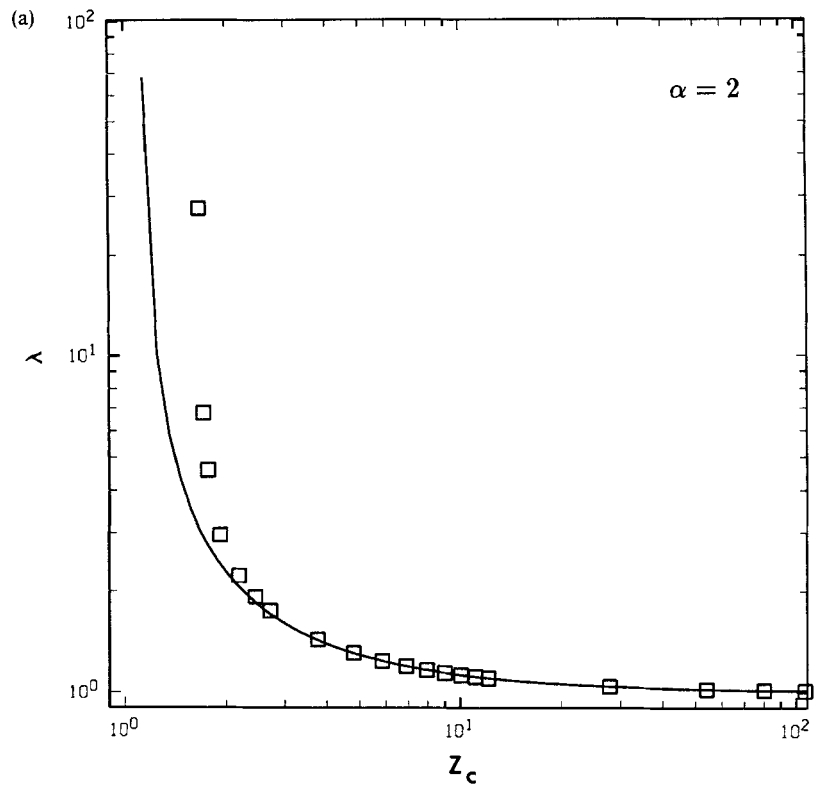

Figure 8. (a) Large-z_c results: □, numerical results for $\alpha = 2$ with 40 elements; ——, asymptotic predictions as given by equation (30)

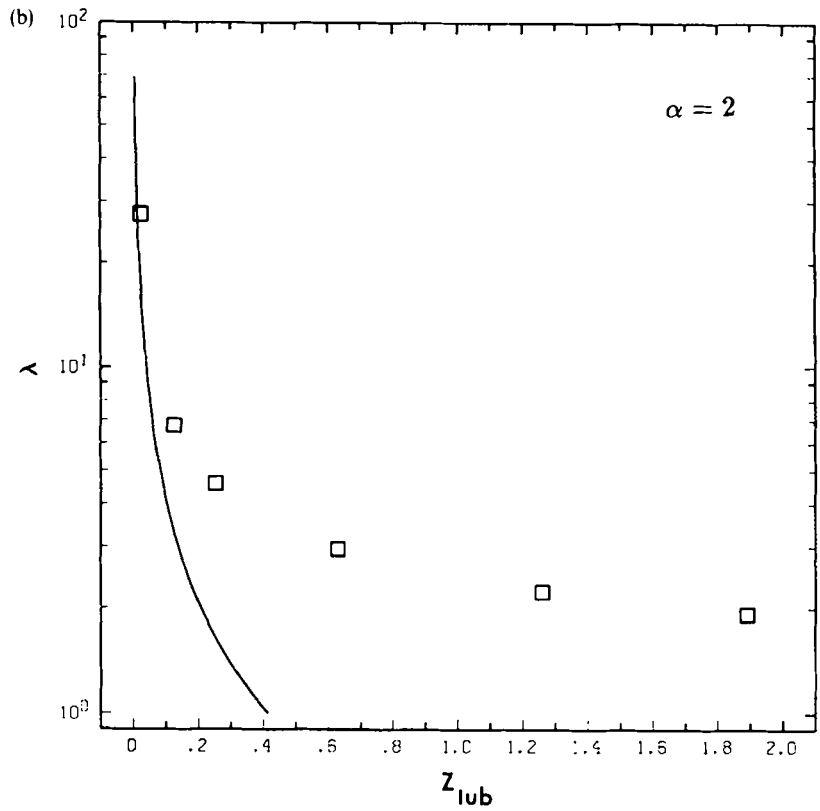

Figure 8. (b) Small-z_{lub} results: □, numerical results for $\alpha = 2$ with 40 elements; ——, Cox's lubrication theory as given by equation (31)

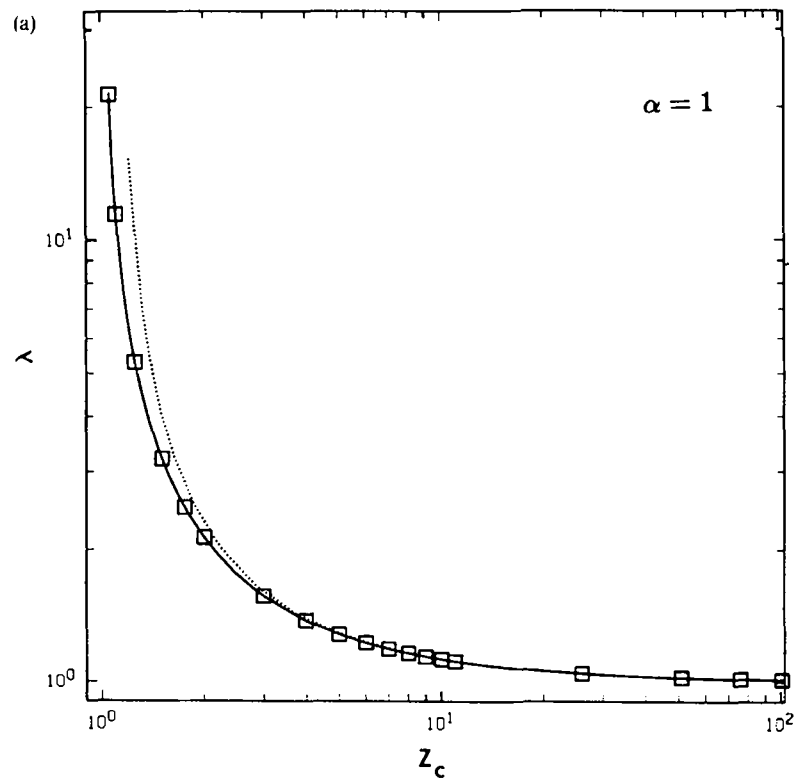

Figure 9. (a) □, numerical results for the sphere case ($\alpha = 1$) with 40 elements; ——, theoretical predictions of Brenner as given by equation (29); · · · · ·, far-field asymptotic predictions as given by equation (30)

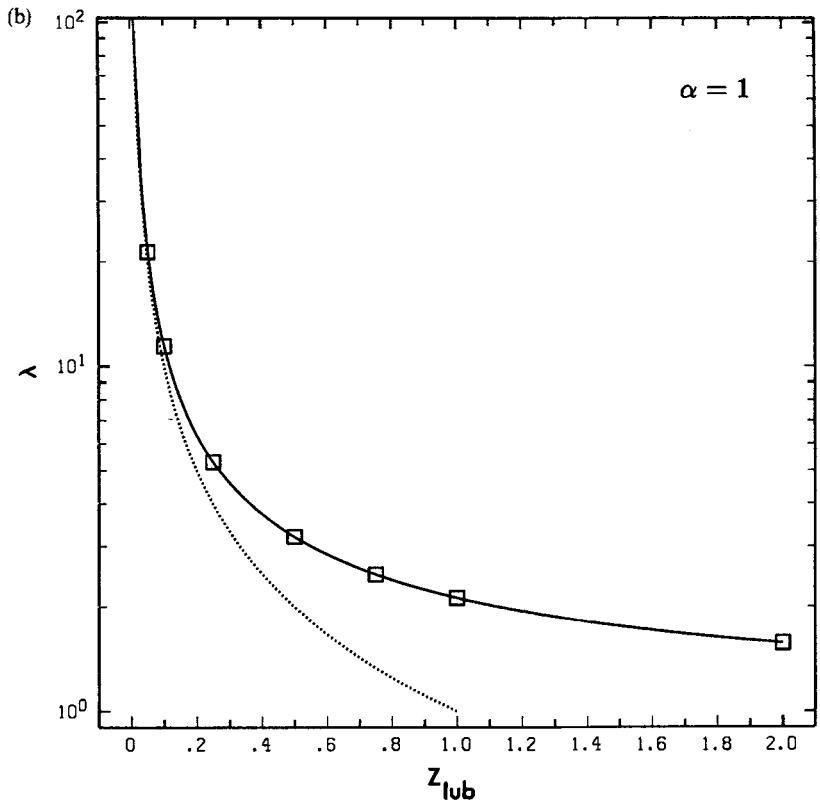

Figure 9. (b) □, numerical results for the sphere case with 40 elements; ——, theoretical predictions of Brenner as given by equation (29); · · · · ·, Cox's lubrication theory as given by equation (31)

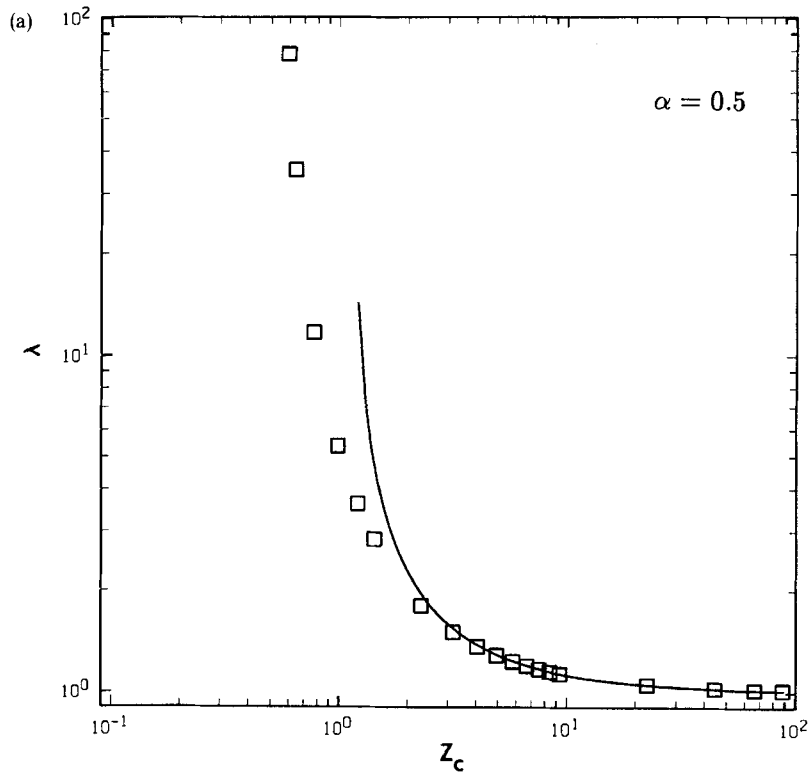

Figure 10. (a) Large-z_c results: □, numerical results for $\alpha = 0{\cdot}5$ with 40 elements; ——, asymptotic predictions as given by equation (30)

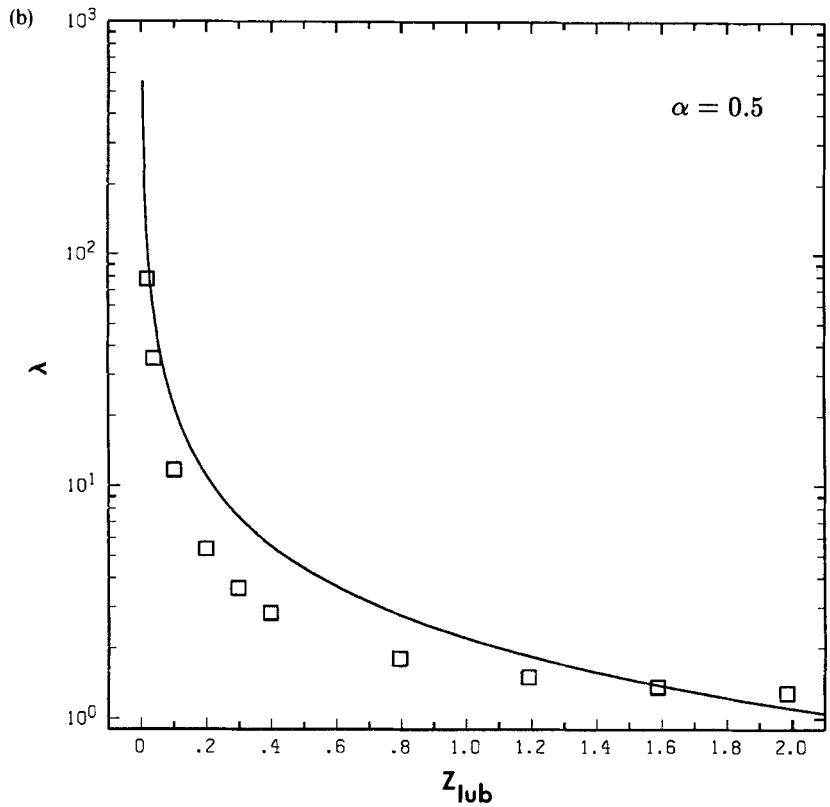

Figure 10. (b) Small-z_{lub} results: □, numerical results for $\alpha = 0{\cdot}5$ with 40 elements; ——, Cox's lubrication theory as given by equation (31)

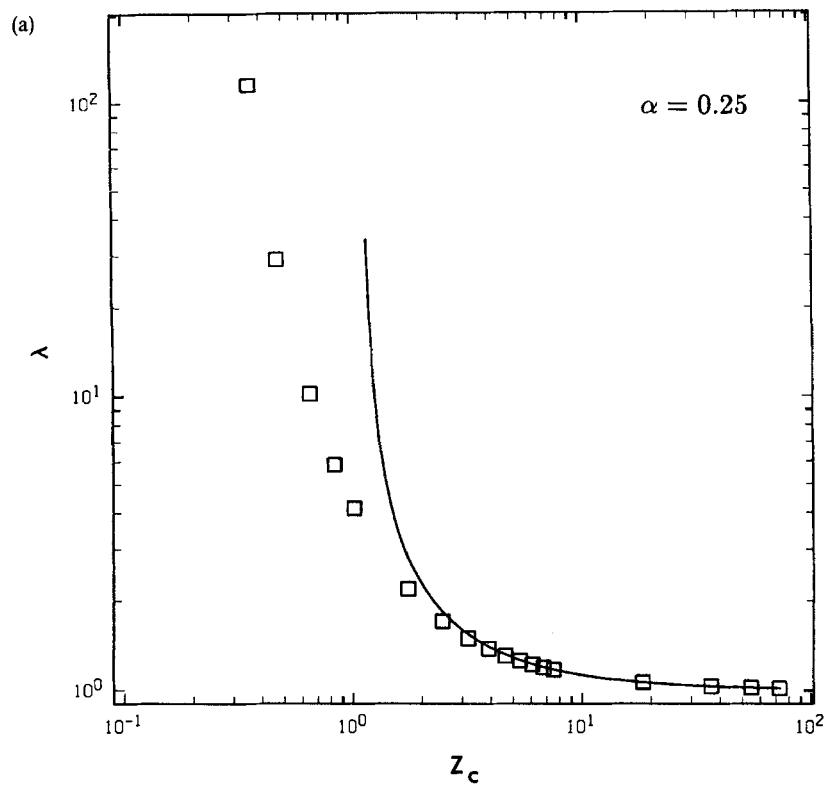

Figure 11. (a) Large-z_c results: □, numerical results for $\alpha = 0{\cdot}25$ with 40 elements; ——, asymptotic predictions as given by equation (30)

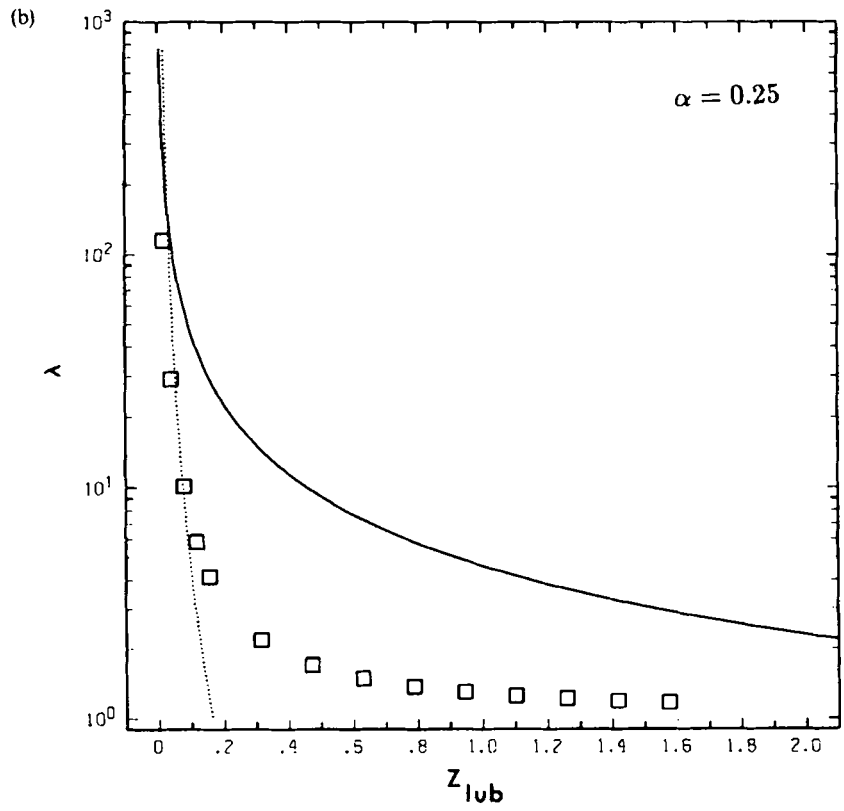

Figure 11. (b) Small-z_{lub} results: □, numerical results for $\alpha = 0{\cdot}25$ with 40 elements; ——, Cox's lubrication theory as given by equation (31); · · · · ·, Reynolds' lubrication theory given by equation (33)

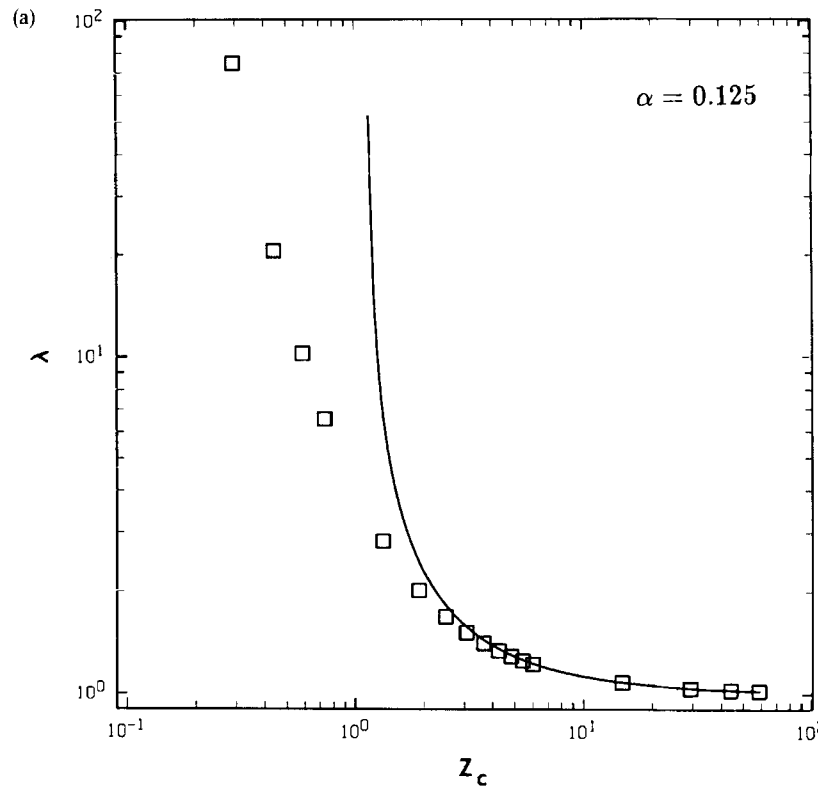

Figure 12. (a) Large-z_c results: □, numerical results for $\alpha = 0{\cdot}125$ with 40 elements; ——, asymptotic predictions as given by equation (30)

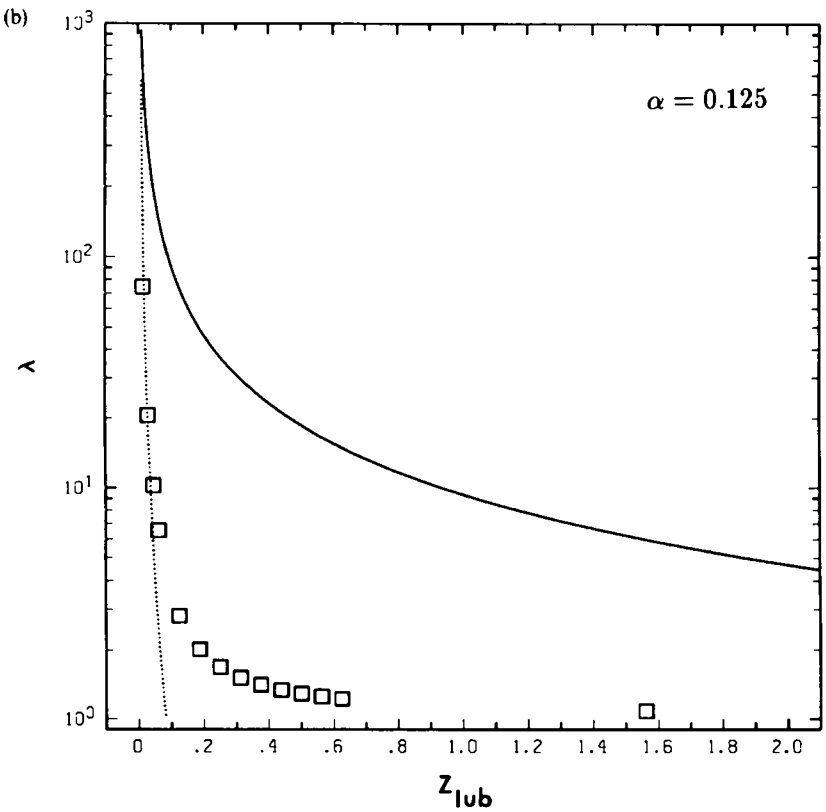

Figure 12. (b) Small-z_{lub} results: □, numerical results for $\alpha = 0{\cdot}125$ with 40 elements; ——, Cox's lubrication theory as given by equation (31); · · · · ·, Reynolds' lubrication theory given by equation (33)

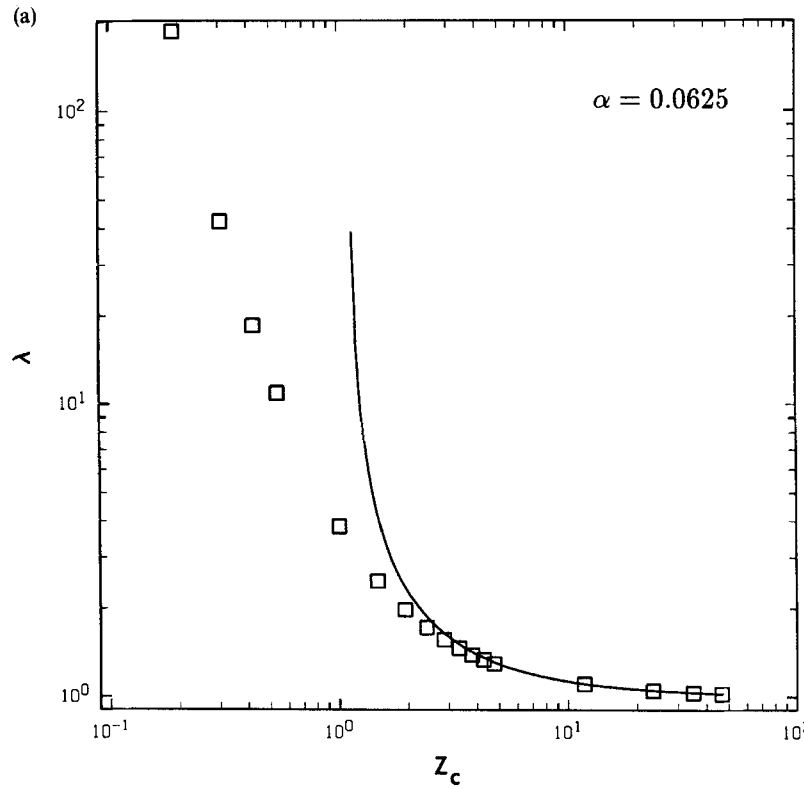

Figure 13. (a) Large-z_c results: □, numerical results for $\alpha = 0{\cdot}0625$ with 40 elements; ——, asymptotic predictions as given by equation (30)

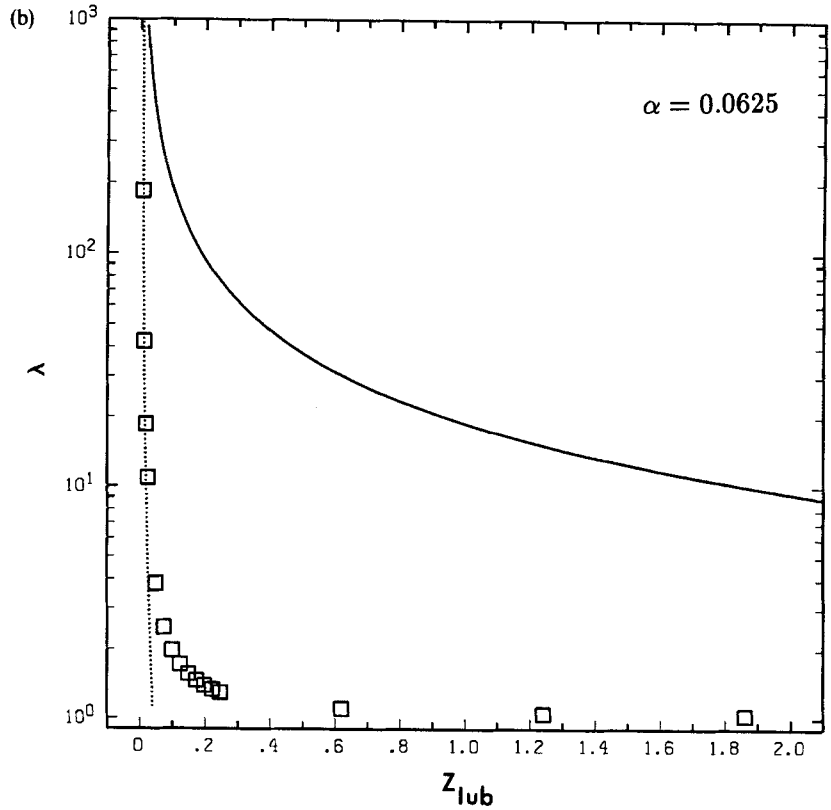

Figure 13. (b) Small-z_{lub} results: □, numerical results for $\alpha = 0{\cdot}0625$ with 40 elements; ——, Cox's lubrication theory as given by equation (31); · · · ·, Reynolds' lubrication theory as given by equation (33)

APPENDIX

The integrals C_p^{nm} and $\hat{C}_p^{nm}$

Using standard integral tables, the integrals denoted by C_p^{nm} and $\hat{C}_p^{nm}$ can be reduced to expressions involving the complete elliptic integrals of the first and second kind given by

$$K(k) = 2\int_0^{\pi} \frac{dx}{[1-k^2\sin^2 x]^{1/2}}, \tag{34}$$

$$E(k) = 2\int_0^{\pi} \frac{dx}{[1-k^2\sin^2 x]^{3/2}}. \tag{35}$$

The final expressions for C_p^{nm} are

$$C_1^{00} = \frac{4}{\gamma^{1/2}} K, \tag{36}$$

$$C_1^{01} = C_1^{00} - \frac{8}{k^2\gamma^{1/2}}(K-E), \tag{37}$$

$$C_3^{00} = \frac{4}{\hat{k}^2\gamma^{3/2}} E, \tag{38}$$

$$C_3^{01} = \frac{4}{k^2\gamma^{3/2}}\left(2K - \frac{1+\hat{k}^2}{\hat{k}^2} E\right), \tag{39}$$

$$C_3^{20} = \frac{16}{k^4\gamma^{3/2}}[(1+\hat{k}^2)K - 2E], \tag{40}$$

$$C_3^{03} = C_3^{01} - C_3^{20} + \frac{32}{3k^6\gamma^{3/2}}[(k^2-8)E + (8-5k^2)K], \tag{41}$$

$$C_5^{00} = \frac{4}{3\hat{k}^2\gamma^{5/2}}\left(\frac{2(1+\hat{k}^2)}{\hat{k}^2} E - K\right), \tag{42}$$

$$C_5^{01} = \frac{4}{3k^2\hat{k}^2\gamma^{5/2}}\left((1+\hat{k}^2)K - \frac{2}{\hat{k}^2}(\hat{k}^2+k^4)E\right), \tag{43}$$

$$C_5^{20} = \frac{16}{3k^4\gamma^{5/2}}\left(\frac{1+\hat{k}^2}{\hat{k}^2} E - 2K\right), \tag{44}$$

$$C_p^{02} = C_p^{00} - C_p^{20}, \tag{45}$$

where

$$\hat{k}^2 = 1 - k^2.$$

The corresponding expressions for $\hat{C}_p^{nm}$ are obtained from the above by replacing γ with γ_R and k with k_R.

Small-k expansions

When k and/or $k_R \to 0$, numerical inaccuracy necessitates the use of asymptotic expansions for the expressions C_p^{nm} and $\hat{C}_p^{nm}$. These asymptotic expansions are obtained by performing a generalized binomial expansion in k^2 on the integrands given in equation (25) and (26). The results, accurate to $O(k^4)$ as $k \to 0$, are

$$C_1^{00} = \frac{2\pi}{\gamma^{1/2}}(1 + \tfrac{1}{8}k^2), \tag{46}$$

$$C_1^{01} = -\frac{\pi k^2}{4\gamma^{1/2}}, \tag{47}$$

$$C_3^{00} = \frac{2\pi}{\gamma^{3/2}}(1 + \tfrac{3}{8}k^2), \tag{48}$$

$$C_3^{01} = -\frac{3\pi k^2}{4\gamma^{3/2}}, \tag{49}$$

$$C_3^{20} = \frac{\pi}{\gamma^{3/2}}(1 + \tfrac{3}{8}k^2), \tag{50}$$

$$C_3^{03} = -\frac{9\pi k^2}{16\gamma^{3/2}}, \tag{51}$$

$$C_5^{00} = \frac{2\pi}{\gamma^{5/2}}(1+\tfrac{5}{8}k^2), \tag{52}$$

$$C_5^{01} = -\frac{5\pi k^2}{4\gamma^{5/2}}, \tag{53}$$

$$C_5^{20} = \frac{\pi}{\gamma^{5/2}}(1+\tfrac{5}{8}k^2). \tag{54}$$

Again the corresponding expressions for $\hat{C}_p^{nm}$ are obtained from the above by replacing γ with γ_R and k with k_R.

The singular contributions

The numerical integration breaks down as $\xi \to \mathbf{x}$ since the kernel becomes unbounded in this case. To include this integrable singular contribution it is necessary to approximate the integral analytically. This is accomplished by Taylor series expanding the singular terms about the point (ρ_o, z_o) in (26). The details involved in carrying out these expansions are analogous to those used by Lee and Leal,[11] the differences being only in the choice of parametrization of the surface. It is important to note, however, that only those terms in the kernel **Q** stemming from the fundamental solution (11) must be considered, since $R \neq 0$ for $z > 0$. Hence we consider the integral

$$\begin{aligned}\mathbf{a} = \int_{s_i-\varepsilon/2}^{s_i+\varepsilon/2}\int_0^{2\pi} \rho[\dot{\rho}^2+\dot{z}^2]^{1/2}\left\{\frac{\mathbf{f}}{r}+\frac{\mathbf{f}\cdot\mathbf{r}}{r^3}\mathbf{r}\right\}\mathrm{d}\theta\,\mathrm{d}s = \int_{s_i-\varepsilon/2}^{s_i+\varepsilon/2}\mathrm{d}s\,\rho[\dot{\rho}^2+\dot{z}^2]^{1/2}\\ \times\{\mathbf{i}[f_\rho C_1^{01}+(\rho^2+\rho_o^2)f_\rho C_3^{01}+\rho\rho_o f_\rho(C_3^{00}+C_3^{02})+f_z r_3(\rho C_3^{01}+\rho_o C_3^{00}]\\ +\mathbf{k}[f_z C_1^{00}+f_\rho r_3(\rho C_3^{00}+\rho_o C_3^{01})+f_z r_3^2 C_3^{00}]\},\end{aligned} \tag{55}$$

where s_i is the value of the arc length parameter of the ith node, and **i** and **k** are the Cartesian base vectors. After carrying out the expansions, the **i**-component of the integral is

$$a_i \simeq 2\varepsilon\left\{f_{z_o}\frac{\dot{\rho}_o\dot{z}_o}{[\dot{\rho}_o^2+\dot{z}_o^2]^{1/2}}+f_{\rho_o}\left[\frac{\dot{\rho}_o^2+2\dot{z}_o^2}{[\dot{\rho}_o^2+\dot{z}_o^2]^{1/2}}-[\dot{\rho}_o^2+\dot{z}_o^2]^{1/2}\ln\left(\frac{\varepsilon}{16\rho_o}[\dot{\rho}_o^2+\dot{z}_o^2]^{1/2}\right)\right]\right\} \tag{56}$$

and the **k**-component is

$$a_k \simeq 2\varepsilon\left\{f_{\rho_o}\frac{\dot{\rho}_o\dot{z}_o}{[\dot{\rho}_o^2+\dot{z}_o^2]^{1/2}}+f_{z_o}\left[\frac{\dot{z}_o^2}{[\dot{\rho}_o^2+\dot{z}_o^2]^{1/2}}+[\dot{\rho}_o^2+\dot{z}_o^2]^{1/2}\left(1-\ln\left(\frac{\varepsilon}{16\rho_o}[\dot{\rho}_o^2+\dot{z}_o^2]^{1/2}\right)\right)\right]\right\}, \tag{57}$$

where the subscript 'o' denotes evaluation at the singular point.

REFERENCES

1. H. Brenner, 'The slow motion of a sphere through a viscous liquid toward a plane surface', *Chem. Eng. Sci.*, **16**, 242 (1961).
2. S. Wakiya, 'Viscous flows past a spheroid', *J. Phys. Soc. Japan*, **12**, 1130–1141 (1957).
3. H. Brenner, 'Effect of finite boundaries on the Stokes resistance of an arbitrary particle', *J. Fluid Mech.*, **12**, 35–48 (1962).
4. H. Brenner, 'Effect of finite boundaries on the Stokes resistance of an arbitrary particle Part 2: Asymmetrical orientations', *J. Fluid Mech.*, **18**, 144–158 (1964).
5. R. G. Cox and H. Brenner, 'Effect of finite boundaries on the Stokes resistance of an arbitrary particle Part 3: Translation and rotation', *J. Fluid Mech.*, **28**, 391–411 (1967).

6. R. G. Cox, 'The motion of suspended particles almost in contact', *Int. J. Multiphase Flow*, **1**, 343–371 (1974).
7. O. Reynolds, *Papers on Mechanical and Physical Subjects, Vol. II*, Cambridge University Press, 1901, pp. 228–310.
8. G. K. Youngren and A. Acrivos, 'Stokes flow past a particle of arbitrary shape: a numerical method of solution', *J. Fluid Mech.*, **69**, 377–403 (1975).
9. O. A. Ladyzhenskaya, *The Mathematical Theory of Viscous Incompressible Flow*, Gordon and Breach, New York, 1963.
10. G. K. Youngren and A. Acrivos, 'On the shape of a gas bubble in a viscous extensional flow', *J. Fluid Mech.*, **76**, 433–442 (1976).
11. S. H. Lee and L. G. Leal, 'Motion of a sphere in the presence of a deformable interface. Part 2: Numerical study of the translation of a sphere normal to an interface', *J. Colloid Interface Sci.*, **87**, 81–106 (1982).
12. J. M. Rallison and A. Acrivos, 'A numerical study of the deformation and burst of a viscous drop in an extensional flow', *J. Fluid Mech.*, **89**, 191–200 (1978).
13. J. R. Blake, 'A note on the image system for a Stokeslet in a no-slip boundary', *Proc. Phil. Soc.*, **70**, 303–310 (1971).
14. C. W. Oseen, *Hydrodynamik*, Akademische Verlagsgesellschaft, 1927.
15. L. V. Kantorovich and V. I. Krylov, *Approximate Methods of Higher Analysis*, Interscience, 1963.
16. H. Lamb, *Hydrodynamics*, Dover, New York, 1945.